processes

MDPI

Article

Original Formation Resistivity Reconstruction and Water-Flooded Zone Identification Using a CNN-BiLSTM-Attention Network

Huiyuan Bian [1], Kun Li [1], Zhibin Lv [2,3,*], Qing Miao [2,3], Jiantuan Jia [2,3] and Fei Wang [4]

[1] College of Geology & Environment, Xi'an University of Science and Technology, Xi'an 710054, China
[2] Qaidam Comprehensive Geological and Mineral Exploration Institute of Qinghai Province, Golmud 816099, China
[3] Qinghai Provincial Key Laboratory of Salt Lake Resource Exploration and Research in Qaidam Basin, Golmud 816099, China
[4] College of Geology Engineering and Geomatics, Chang'an University, Xi'an 710054, China
* Correspondence: lvzhibin198784@163.com

Abstract

Reliable identification and assessment of water-flooded intervals are crucial for enhancing oil recovery during the middle and late stages of field development. Original formation resistivity is an important parameter characterizing the initial electrical properties of a reservoir and provides a critical basis for water-flooded zone identification and remaining-oil evaluation. To overcome the limited accuracy and robustness of conventional inversion approaches in complex reservoirs, this study develops a CNN-BiLSTM-Attention framework for reconstructing original formation resistivity. CNN captures local variations in the logging responses and BiLSTM models' bidirectional dependencies along the depth sequence, and the attention module highlights informative representations, thereby strengthening nonlinear characterization and model robustness. The Yuejin II Oilfield in the western Qaidam Basin was selected as the study area, and conventional logging data were used for model development and independent assessment. The proposed framework achieved better reconstruction performance than the comparison models. Based on the reconstructed resistivity, a resistivity attenuation ratio M was introduced and integrated with conventional logging parameters to distinguish different water-flooding levels. The integrated M+GR+AC classification scheme reached 93.6%. These results demonstrate that combining deep-learning-based resistivity reconstruction with conventional logging parameters can improve the reliability of water-flooded zone identification in complex heterogeneous reservoirs and provide technical support for remaining-oil evaluation and refined development of high water-cut oilfields.

Keywords: deep learning; CNN-BiLSTM-Attention; well-log reconstruction; attention mechanism; water-flooded zone identification

Check for updates

Academic Editor: Youguo Yan

Received: 2 September 2026
Revised: 11 October 2026
Accepted: 16 October 2026
Published: 6 November 2026

Copyright: © 2026 by the authors. Licensee MDPI, Basel, Switzerland. This article is an open access article distributed under the terms and conditions of the Creative Commons Attribution (CC BY) license.

1. Introduction

Resistivity logs provide essential information for fluid identification and water-saturation evaluation in reservoir formations. Its response characteristics therefore have a substantial influence on the accuracy of reservoir evaluation [1]. As an oilfield enters the high water-cut stage of development, the properties and spatial distribution of formation fluids change markedly. The original oil phase is gradually replaced by injected water, which generally causes formation resistivity to decrease and produces increasingly complex

electrical responses in both the vertical and radial directions [2]. The resistivity measured by well logging reflects not only the current fluid distribution but also the effects of mud invasion, changes in flushed-zone resistivity, and dynamic reservoir evolution during long-term production. Consequently, the measured apparent resistivity may deviate from the original formation resistivity [3]. This problem becomes particularly pronounced in strongly water-flooded reservoirs or wells subjected to repeated injection and production operations, where resistivity curves may exhibit low-resistivity smoothing, reduced curve variability, poorly defined formation boundaries, or anomalous fluctuations. Such responses make it more difficult to identify remaining oil and to determine the intensity of water flooding. Therefore, estimating the resistivity characteristics of the reservoir under unflooded reference conditions is important for interpreting water-flooded intervals. In this context, the estimated reference resistivity provides a baseline against which the present-day measured resistivity can be compared. However, the estimated baseline should be distinguished from the actual historical pre-flooding resistivity, which may not be directly available from present-day logging measurements. Methods such as environmental correction, invasion-profile inversion, and data-driven prediction can help reconstruct electrical properties that are closer to the original formation state or initial oil-bearing condition, thereby improving the robustness of detailed water-flooded zone evaluation [4,5].

With recent advances in machine learning, increasing attention has been devoted to data-driven reconstruction of well-log responses, and promising results have been achieved. Extensive applications have demonstrated that machine learning methods offer flexible parameterization and broad applicability compared with many conventional approaches, promoting their increasing use in well-log reconstruction [6]. Long short-term memory (LSTM) models have been employed for reconstructing missing logging curves, including resistivity, by modeling sequential dependencies within logging data. These methods have achieved substantially better reconstruction performance than conventional interpolation and fully connected neural networks [7]. XGBoost ensemble learning has also been used for well-log reconstruction. Applications in the Bohai Bay Basin have shown that XGBoost provides greater stability and generalization capability than methods such as gradient boosting decision trees (GBDT), random forests (RF), and feedforward neural networks (FNN) [8]. Deep learning models combining cascaded bidirectional LSTM (BiLSTM) networks with residual attention mechanisms have further improved the reconstruction accuracy of long well-log sequences, including resistivity curves [9]. Recent Transformer-based approaches have also been investigated for well-log reconstruction, including domain-adaptive reconstruction of missing logs and high-fidelity resistivity prediction [10,11]. Liu et al. further developed a reconstruction workflow targeting deep laterolog resistivity at a vertical resolution of 0.2 m [12]. The workflow combines XGBoost prediction with systematic bias correction in thick layers, and crossplot analysis was used to verify its effectiveness for fluid identification. The approach demonstrated strong predictive performance in practical applications and represents a recent approach to high-resolution resistivity reconstruction in thinly interbedded formations. For reconstruction based on inversion of invasion profiles and true formation resistivity, Ge et al. proposed a hybrid inversion algorithm combining Markov chain Monte Carlo (MCMC) global sampling with Levenberg–Marquardt local optimization [13]. Based on a five-parameter formation resistivity model, the method retrieves original formation resistivity and flushed-zone parameters from array induction logging data, improving the robustness and reliability of resistivity reconstruction under complex invasion conditions. In addition, for the recovery of electrical properties in cased wells, Sheng et al. systematically investigated the influence of source-receiver spacing on signal separation and formation conductivity estimation using transient electromagnetic measurements through casing, providing a methodological basis for reconstructing electrical logs under cased-hole conditions [14].

To address the strong nonlinearity, pronounced sequential dependence, and difficulty in identifying key features during original formation resistivity reconstruction in complex reservoirs, a CNN-BiLSTM-Attention framework was constructed [15]. In this architecture, CNN is used to capture local patterns from the logging inputs, BiLSTM learns contextual dependencies in both directions along the depth sequence, and the attention module assigns greater importance to informative representations [16,17]. Through this integrated architecture, the model enables efficient and accurate reconstruction of the original formation resistivity. The major contribution of this study is the development of a reconstruction-assisted framework for water-flooding interpretation. The framework uses the estimated unflooded reference resistivity to characterize resistivity variations through the attenuation ratio M. By integrating M with GR and AC, the framework establishes a quantitative link between resistivity reconstruction and water-flooding intensity identification.

2. Geological Setting

2.1. Regional Tectonic Setting and Characteristics

The experimental study area for water-flooded zone analysis is located in the western Qaidam Basin, with Well Yuejin II in the eastern high structural block of the Yuejin II Oilfield selected as the research target.The regional location and tectonic setting of the Yuejin II Oilfield in the western Qaidam Basin are shown in Figure 1. Structurally, the study area is situated within the Kunbei fault-step subzone of the Tiemulike uplift in the western depression of the Qaidam Basin, which represents a third-order structural unit in this region. The study area has experienced the superposition of multiple tectonic events, resulting in a complex structural framework. The deep formations are mainly characterized by compressional deformation, whereas the shallow formations are dominated by extensional deformation. The fault system exhibits distinct vertical stratification characteristics, with thrust faults mainly developed in the deeper intervals and normal faults prevailing in the shallow strata.

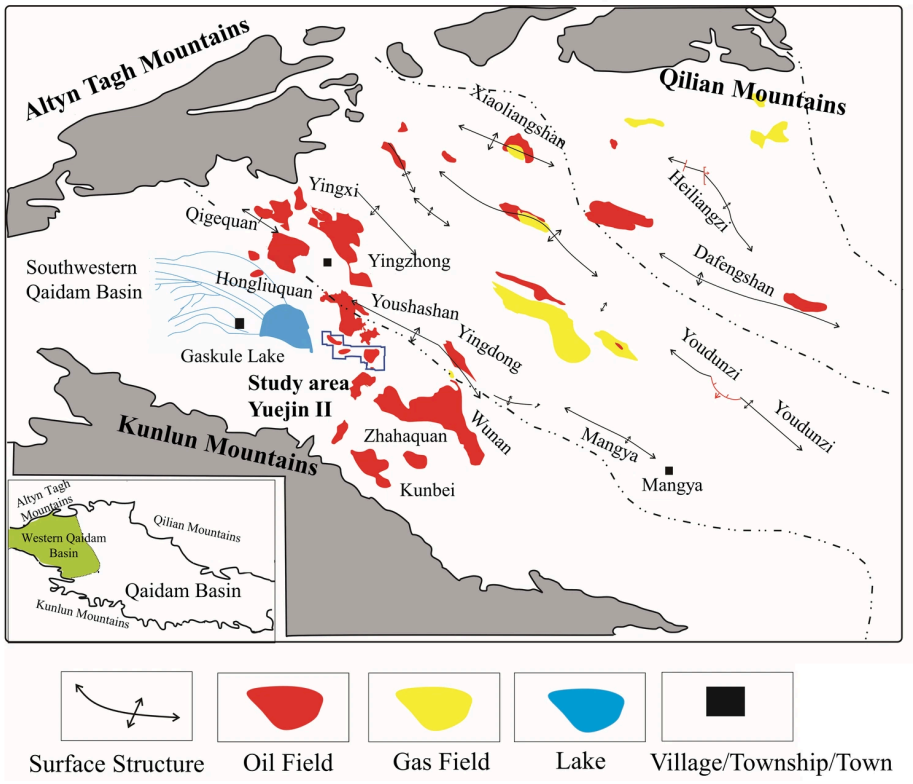


Figure 1. Regional location and tectonic setting of the Yuejin II Oilfield in the western Qaidam Basin, China.

2.2. Lithological and Petrophysical Characteristics

The lithologic compositions and shale-content distributions of the N_2^1 and N_1 reservoirs are shown in Figure 2. The N_2^1 and N_1 reservoirs in the Yuejin II Oilfield are mainly composed of clastic sediments, but their lithological assemblages vary between different stratigraphic intervals. The N_2^1 reservoir is dominated by medium-grained sandstone, accounting for approximately 26%, followed by siltstone and fine-grained sandstone, each of which accounts for around 20%. In addition, argillaceous sandstone and argillaceous siltstone are also developed in this interval, with a small amount of gravel-bearing sandstone locally occurring. These characteristics indicate that the hydrodynamic conditions of the depositional environment experienced certain variations. Overall, the N_2^1 reservoir is characterized by moderate sandstone grain size and relatively developed argillaceous components. The lithological composition of the N_1 reservoir is more complex, with mudstone being the dominant lithology, accounting for nearly 40% [18]. Mudstone is a fine-grained clastic sedimentary rock; the reported proportion describes the lithological composition of the N_1 succession rather than the proportion of productive reservoir intervals. It is followed by gravelly siltstone and argillaceous sandstone, while sandstone lithologies account for a relatively smaller proportion. These features suggest that the depositional environment of the N_1 reservoir was characterized by relatively low energy conditions, resulting in the extensive accumulation of fine-grained sediments.

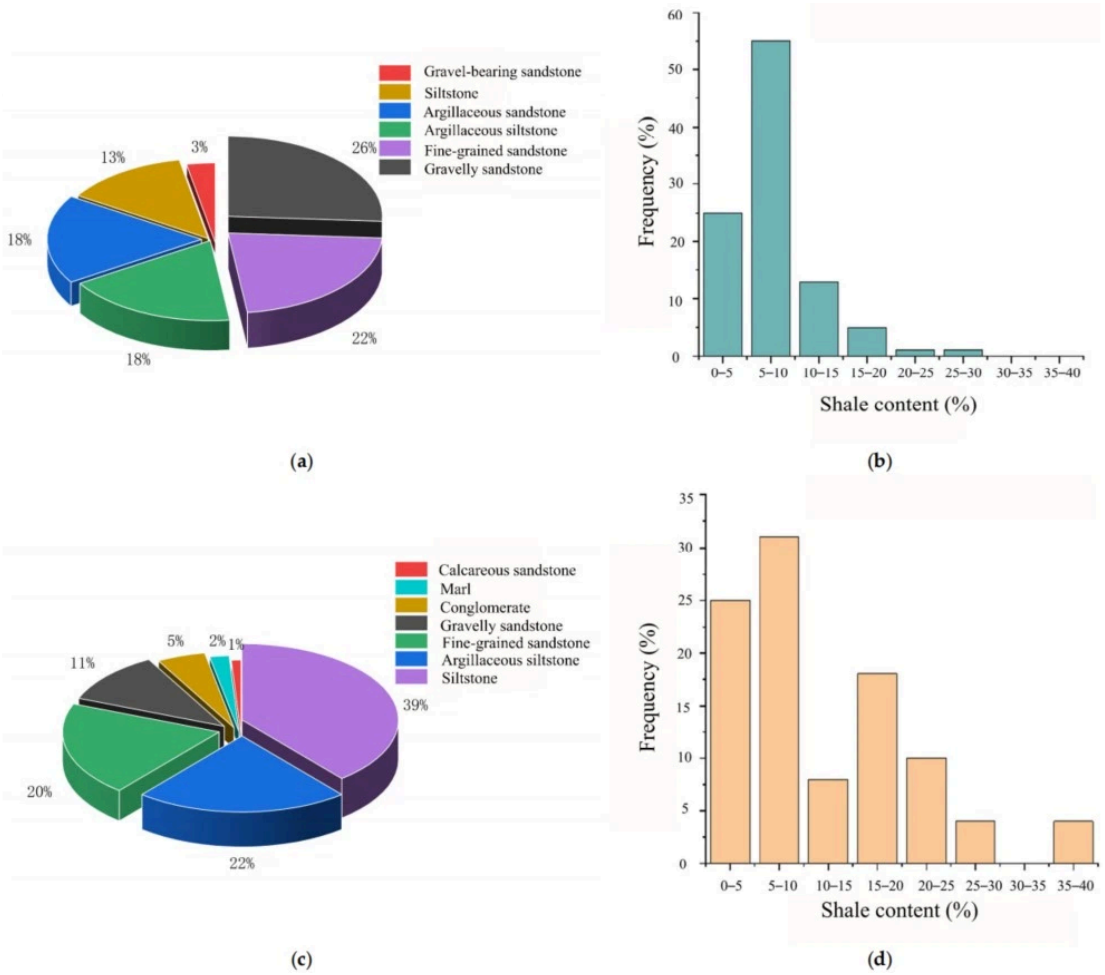


Figure 2. Lithologic composition and shale content distribution of the N_2^1 and N_1 reservoirs in the Yuejin II Oilfield. (**a**) Lithologic composition of the N_2^1 reservoir (**b**) Histogram of shale content in the N_2^1 reservoir (**c**) Lithologic composition of the N_1 reservoir (**d**) Histogram of shale content in the N_1 reservoir.

The statistical distributions of porosity and permeability across the study area are shown in Figure 3. A comparison of the two reservoir intervals shows an overall upward transition from medium-grained sandstone in the N_2^1 reservoir to finer-grained clastic rocks in the N_1 reservoir. The distribution of argillaceous components also varies markedly between the two intervals. These lithological changes reflect vertical variations in depositional energy and sediment supply and, to some extent, influence the distribution of reservoir petrophysical properties. Based on core analyses from the entire oilfield, a total of 427 porosity measurements were obtained, with an average porosity of 16.76%. The porosity distribution is mainly concentrated between 15% and 25%. Permeability was measured from 376 core samples, yielding a geometric mean of 18.7×10^{-3} μm^2, with most values ranging from 100 to 1000×10^{-3} μm^2. The average residual oil saturation is 30.83%, and the dominant distribution range is 30% to 35%. Overall, the reservoirs show generally moderate-to-low porosity and permeability.

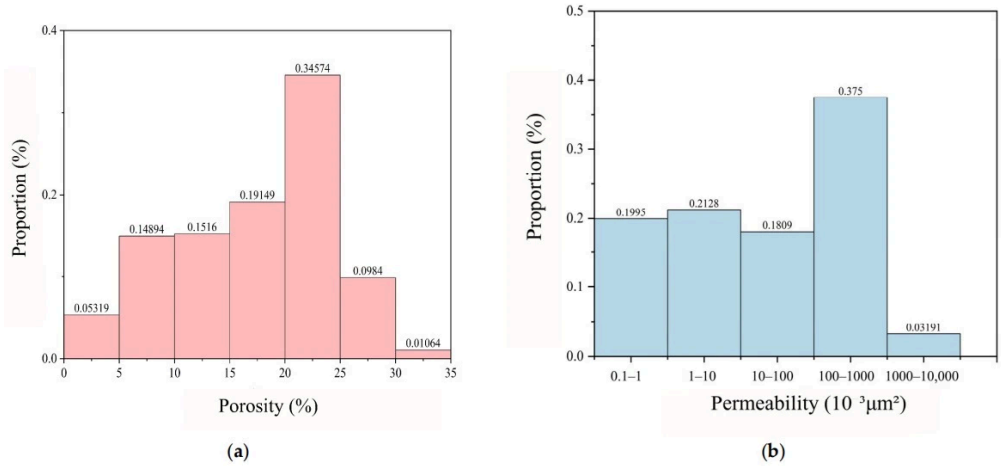


Figure 3. Statistical distributions of reservoir petrophysical properties in the study area. (**a**) Porosity distribution of the entire oilfield (**b**) Permeability distribution of the entire oilfield.

2.3. Logging Response Characteristics

During reservoir development, the invasion of formation water alters the original fluid distribution within the reservoir and consequently affects the responses of logging curves. Therefore, the identification and evaluation of water-flooded zones are important components of production logging interpretation. Crossplot analysis combines logging parameters that are sensitive to changes in reservoir fluids and provides an intuitive way to characterize logging responses under different fluid conditions. This method has therefore been widely used for water-flooded zone identification.

During waterflooding, hydrocarbons in the reservoir pores are gradually displaced by formation water, leading to changes in pore-fluid composition and corresponding variations in the electrical properties of the reservoir. Among the available logging responses, resistivity is particularly sensitive to waterflooding. In general, unflooded oil-bearing zones exhibit relatively high resistivity, whereas water-bearing zones show lower resistivity. Reservoir intervals affected by different degrees of waterflooding typically have resistivity values between those of oil-bearing and water-bearing zones, where resistivity tends to decline with increasing water-flooding intensity. Therefore, resistivity can serve as an effective indicator for evaluating the degree of reservoir water flooding. Crossplots are interpretation charts used to characterize relationships between logging parameters based on their response patterns. Considering the differences in logging responses at different stages of waterflooding, formation resistivity R_t was crossplotted against conventional logging

parameters, including compensated neutron porosity, acoustic transit time, density, and gamma ray. Accordingly, CNL-R_t (Figure 4a), AC-R_t (Figure 4b), DEN-R_t (Figure 4c), and GR-R_t (Figure 4d) crossplots were established for water-flooding discrimination. The results show that both gamma ray and resistivity generally decrease after waterflooding, with resistivity exhibiting a more pronounced response. Under waterflooding conditions, acoustic transit time increases slightly, whereas resistivity decreases markedly, and lower resistivity values are generally associated with stronger waterflooding. In contrast, density shows relatively limited sensitivity to changes caused by waterflooding and therefore provides weaker discrimination. Variations in CNL among different reservoir types are also relatively small, with most data points concentrated within approximately 25% to 35%, indicating limited differences in overall porosity and relatively similar lithological conditions in the study area. As waterflooding becomes more intense, CNL shows a slight increasing trend. This response may be related to water flushing, which reduces surface and intergranular filling materials, enlarges pore throats, increases porosity, and raises the water content of the reservoir, resulting in higher compensated neutron readings.

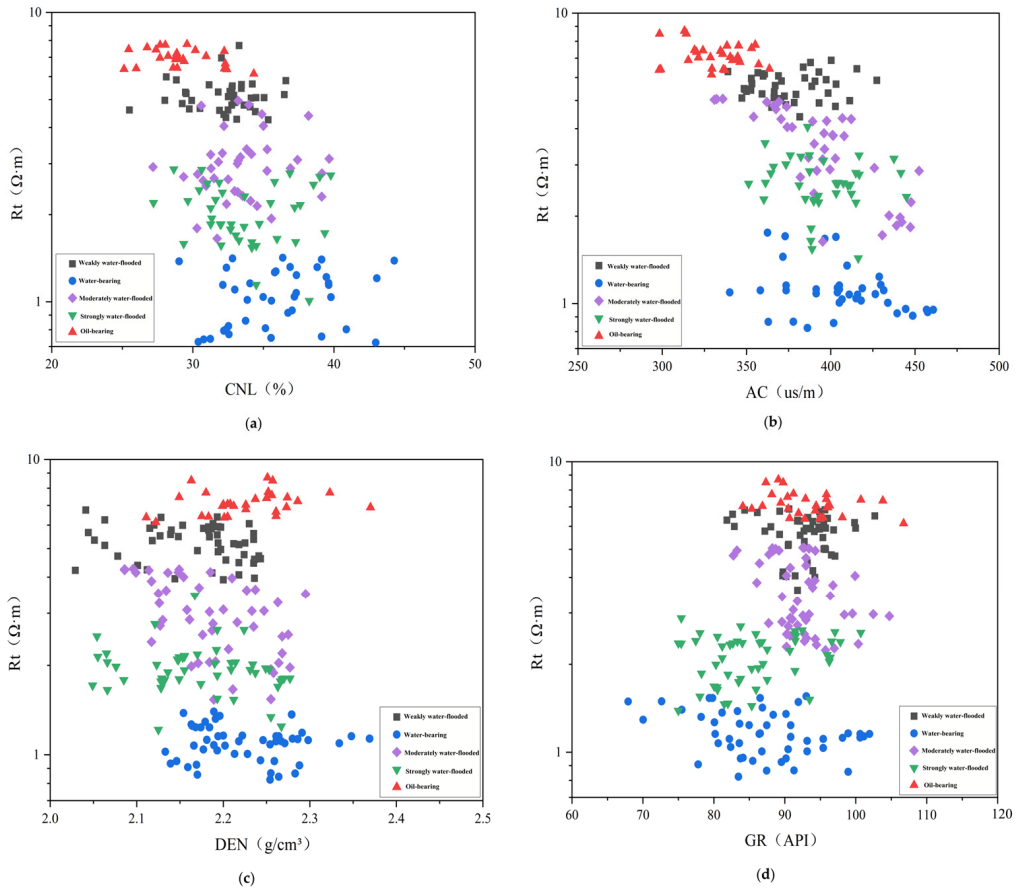


Figure 4. Crossplot-based identification of water-flooded zones. (**a**) CNL-R_t crossplot (**b**) AC-R_t crossplot (**c**) DEN-R_t crossplot (**d**) GR-R_t crossplot.

3. Intelligent Identification of Water-Flooded Zones Based on Deep Learning Reconstruction of Reservoir Resistivity

3.1. Principle of the Hybrid Model

To address the challenges associated with reconstructing original formation resistivity in complex reservoirs, including strong nonlinear relationships, pronounced sequence dependence, and difficulty in identifying key features, a CNN-BiLSTM-Attention hybrid

deep learning framework was constructed. The proposed framework uses CNN to extract local features, BiLSTM to learn bidirectional dependencies along the depth sequence, and an attention module to emphasize informative representations. This combination enables accurate and efficient reconstruction of the original formation resistivity.

(1) Bidirectional Long Short-Term Memory Network

Bidirectional long short-term memory (BiLSTM) extends the traditional LSTM structure and is well suited for extracting sequential characteristics from logging data [19]. BiLSTM processes the logging sequence in both directions, allowing information from the intervals above and below each target depth to contribute to feature learning and thereby improving the representation of depth-wise dependencies [20].

As shown in Figure 5, the LSTM unit forms the core of the BiLSTM network and uses gated operations to control the transmission of information. The LSTM unit forms the core of the BiLSTM network and uses gated operations to control the transmission of information. The input and forget gates are responsible for updating newly received information and previous states, whereas the output gate determines the information transferred to the hidden layer [21]. This gated structure helps preserve useful sequential information and alleviates gradient degradation during long-range dependency modeling.

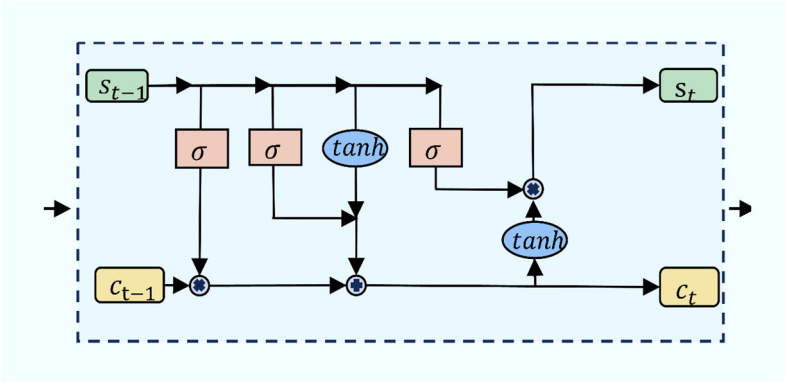


Figure 5. Structure of the LSTM gating mechanism.

BiLSTM extends conventional LSTM by learning the logging sequence in two directions. The forward branch captures information from shallower to deeper intervals, whereas the backward branch incorporates information from the opposite direction. Their representations are subsequently fused, enabling the model to exploit geological context on both sides of each target depth and improving the characterization of depth-dependent logging variations [4].

The hyperbolic tangent (tanh) function is used within the BiLSTM layers to support nonlinear sequence representation. For sequence position t in the BiLSTM network, d denotes the processing direction. The corresponding hidden state and cell state are represented by ${i_t}^d$ and ${c_t}^d$, respectively:

Input gate (${i_t}^d$):

$$i_t^d = \sigma(W_i^d \cdot [h_{t-d}, x_t] + b_i^d) \quad (1)$$

Forget gate (${f_t}^d$):

$$f_t^d = \sigma(W_f^d \cdot [h_{t-d}, x_t] + b_f^d) \quad (2)$$

Output gate (${o_t}^d$):

$$o_t^d = \sigma(W_o^d \cdot [h_{t-d}, x_t] + b_o^d) \quad (3)$$

Cell state update (${C_t}^d$):

$$\tilde{C}_t^d = \tanh(W_C^d \cdot [h_{t-d}, x_t] + b_C^d) \quad (4)$$

$$C_t^d = f_t^d \cdot C_{t-d} + i_t^d \cdot \tilde{C}_t^d \quad (5)$$

Hidden state update ($h_t{}^d$):

$$h_t^d = o_t^d \cdot \tanh(C_t^d) \quad (6)$$

The architecture of the BiLSTM network is illustrated in Figure 6. During model training, overfitting may occur when the training dataset is limited, the data contain substantial noise, or the network structure is overly complex. To reduce this risk, dropout is introduced into the BiLSTM network. During training, dropout randomly deactivates a subset of neurons and their connections in each iteration, while a different subset is deactivated in the next iteration. As a result, the network structure used for training changes continuously across iterations, which reduces excessive dependence on specific neurons and improves model generalization. From another perspective, dropout can be regarded as repeatedly sampling different sparse subnetworks from the original network during training. Dropout randomly suppresses part of the network activations, reducing excessive dependence on specific neurons and improving generalization to unseen data. The schematic illustration of the dropout technique before and after dropout is shown in Figure 7. The dropout operation can be expressed as follows:

$$\text{Dropout}(f(W_d \cdot \text{mask}(h_l) + b_d)) \quad (7)$$

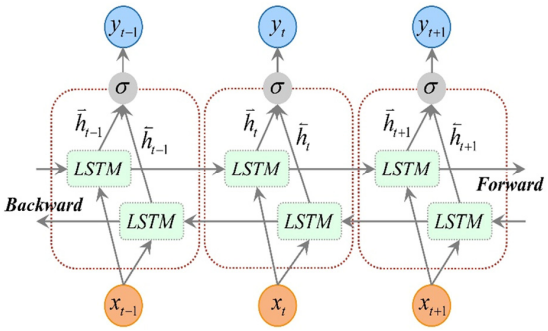


Figure 6. Architecture of the BiLSTM network.

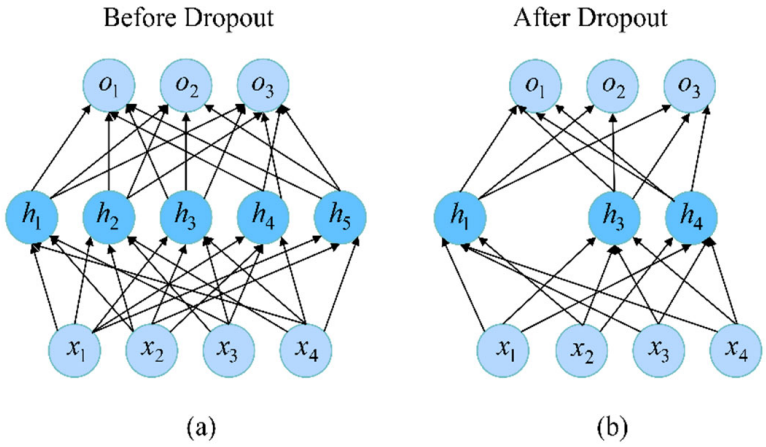


Figure 7. Schematic illustration of the dropout technique: (**a**) before dropout; (**b**) after dropout.

(2) CNN

CNNs are effective for extracting local patterns from sequential data [22]. In this study, CNN is employed to capture local variations in the logging curves before the extracted representations are passed to the subsequent sequence-modeling module. The architecture

of the convolutional network is illustrated in Figure 8 [23].Different colors are used to visually distinguish the network components, including the input, 1D convolution, pooling, flattening, and output layers.

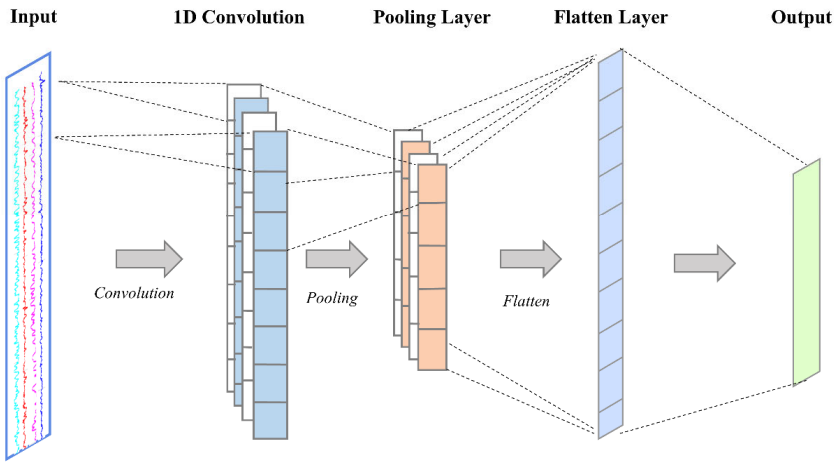


Figure 8. Schematic architecture of the CNN.

Within the network, the convolutional layer plays a central role in extracting effective local characteristics from the input signals. During convolution, a kernel, or filter, moves across the input sequence with a predefined stride and performs weighted calculations over local regions. With convolution kernels of various sizes, the network is able to extract features from different spatial scales [24]. As the network becomes deeper, increasingly complex feature patterns can be learned, allowing the model to extract information progressively from simple local responses to higher-level representations [7]. The convolution operation is expressed as follows:

$$y(i,j) = (x * w)(i,j) = \sum_{m} \sum_{n} x(m,n) \cdot w(i-m, j-n) \tag{8}$$

The convolution outputs are transformed by a nonlinear activation function before entering the next stage of the network. In this study, the ReLU function is selected because it offers an effective nonlinear transformation and contributes to stable network optimization. Its expression is given as follows:

$$\mathrm{ReLU}(f(h_l)) = \max(0, h_l) \tag{9}$$

Pooling is subsequently performed to compress the learned representations and reduce computational complexity. It also makes the extracted local patterns less sensitive to small variations along the logging sequence, thereby improving feature stability. The commonly used pooling strategies include max pooling and average pooling, whose calculation processes are defined as follows:

$$y(i,j) = \max_{(m,n) \in \mathrm{pool}} x(m,n) \tag{10}$$

Through the sequential operations of convolution, activation, and pooling, a CNN progressively extracts and represents features from the input data. The convolutional layers capture local structural patterns, while the pooling operations reduce feature dimensionality and improve model stability without imposing excessive computational cost. By stacking multiple network layers, the CNN can learn increasingly representative features from the original data and provide effective feature representations for subsequent prediction and analysis.

(3) Attention Mechanism

Although CNN-BiLSTM can capture local patterns and sequential dependencies in logging data, some task-relevant information may still be insufficiently represented under complex reservoir conditions. To enhance the use of informative sequence features, a multi-head attention module is incorporated after the BiLSTM layers [25]. The module adaptively emphasizes more relevant representations while suppressing less useful information, thereby improving the robustness and accuracy of well-log reconstruction [20,26].

Compared with conventional single-head attention, multi-head attention can learn feature representations simultaneously in multiple subspaces. By introducing several parallel attention heads, the model can analyze the input information from different perspectives and obtain richer feature representations [20]. Each attention head performs an independent attention calculation and attends to distinct regions of the input sequence. The resulting representations are fused to provide a more comprehensive description of the sequence, which is beneficial for modeling complex logging responses [3]. The multi-head attention operation is defined as follows:

$$\text{Attention}(Q, K, V) = \text{softmax}\left(\frac{QK^T}{\sqrt{d_k}}\right)V \tag{11}$$

The BiLSTM outputs are mapped into several representation subspaces and processed by parallel attention heads. It should be noted that the attention scores generated by the multi-head attention module represent the internal weighting of learned sequence representations rather than direct physical contributions of the original logging variables. The resulting features are then fused to form a unified representation for subsequent prediction. This multi-head design enables the network to learn complementary relationships in the logging sequence and improves the representation capability for complex logging responses (Figure 9).

The CNN-BiLSTM-Attention framework is developed to estimate original formation resistivity from conventional logging data. CNN captures local variations in the logging curves, while BiLSTM models depth-dependent relationships between adjacent intervals. The attention module further emphasizes informative sequence representations. By combining these complementary components, the model improves the characterization of nonlinear logging responses and provides a more reliable basis for subsequent water-flooded zone identification [27].

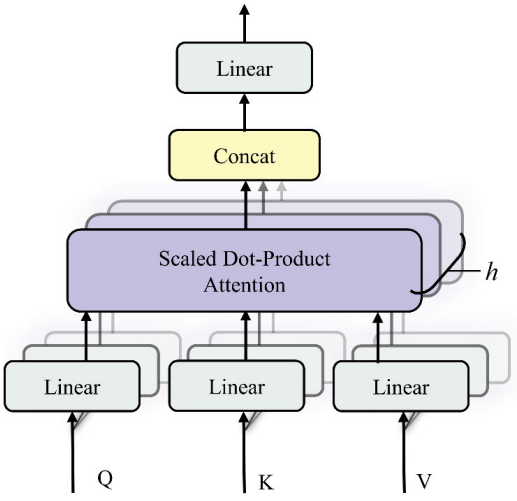


Figure 9. Schematic diagram of the attention mechanism.

3.2. CNN-BiLSTM-Attention Model

The architecture adopted for original formation resistivity reconstruction is illustrated in Figure 10. It includes five successive stages: logging-data input, CNN-based local feature extraction, BiLSTM-based sequence learning, multi-head attention, and resistivity prediction [28]. The functions of these components are described as follows.

1. Input layer. After preprocessing and normalization, the logging sequences are organized into model-ready samples and supplied to the network.
2. CNN layers. One-dimensional convolution is applied along the depth sequence to capture local variations in the logging responses. The convolutional features are activated by ReLU and compressed through max pooling before being transferred to the BiLSTM module.
3. BiLSTM layers. The CNN-derived representations are processed bidirectionally to capture dependencies between neighboring and surrounding depth intervals.
4. Multi-head attention layer. Multi-head attention is applied to the BiLSTM representations to highlight information that contributes most strongly to resistivity reconstruction and to integrate complementary sequence dependencies.
5. Output layer. At the final stage, the output layer transforms the features extracted and refined by the preceding layers into the final prediction result.

To improve model robustness, data augmentation, regularization, and hyperparameter tuning were incorporated into the training procedure. Sliding-window sampling and controlled perturbations were used to increase sample diversity and improve adaptability to different formation conditions. Random perturbations were applied only to the training subset, while the validation and testing datasets remained unchanged. Regularization was additionally applied to limit overfitting and enhance prediction stability on unseen data [29].

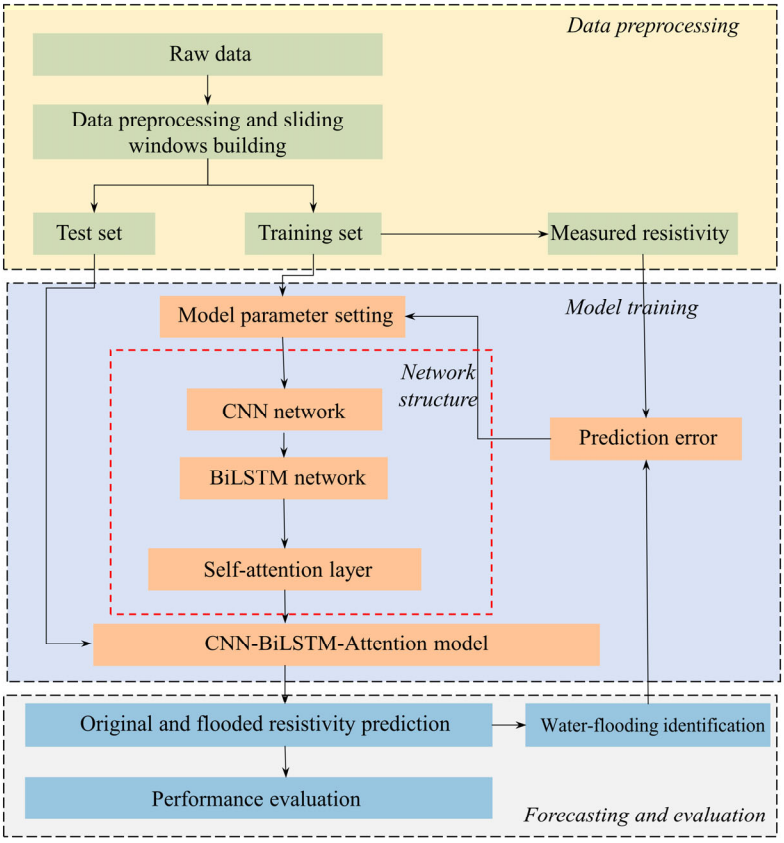


Figure 10. Technical workflow for resistivity reconstruction.

For hyperparameter tuning, Bayesian optimization was adopted to determine an appropriate hyperparameter configuration. A Gaussian-process surrogate was used to approximate the relationship between candidate parameter settings and model performance, allowing subsequent trials to be selected according to information obtained from previous evaluations. Therefore, an approximate optimal configuration can be achieved within a limited number of optimization steps. Unlike traditional grid search and random search methods, Bayesian optimization makes use of previous evaluation results to guide subsequent sampling, thereby improving search efficiency and reducing computational cost. At each iteration, the next candidate configuration is determined by an acquisition function that balances the potential for performance improvement against the uncertainty of the surrogate model. The acquisition function is presented in Equation (12).

$$\alpha(x) = Acquisition\ Function \tag{12}$$

The candidate with the greatest expected benefit is selected for the next iteration, as described in Equation (13).

$$x_{next} = \text{argmax}_x \alpha(x) \tag{13}$$

The expected improvement (EI) criterion is adopted to quantify the improvement over the current best solution based on the predicted value and to standardize this difference. The corresponding expression is given in Equation (14).

$$EI(x) = \mathbf{E}\left[\max(0, f(x) - f(x_{\text{best}}))\right] \tag{14}$$

Bayesian optimization was performed using the validation subset of the model-development well for hyperparameter evaluation. For each candidate hyperparameter configuration, the model was optimized using the training subset, and its performance was assessed according to the validation mean squared error. The parameter combination with the minimum validation error was chosen for the final model training and performance assessment. The optimization procedure involved 30 iterations. The best validation MSE stabilized during the final 5 iterations, indicating convergence within the adopted search budget. The independent evaluation and additional validation wells were excluded from the hyperparameter search.

Figure 11 summarizes the complete framework, including data input, CNN-based feature extraction, BiLSTM sequence modeling, attention refinement, resistivity output, and Bayesian hyperparameter optimization.

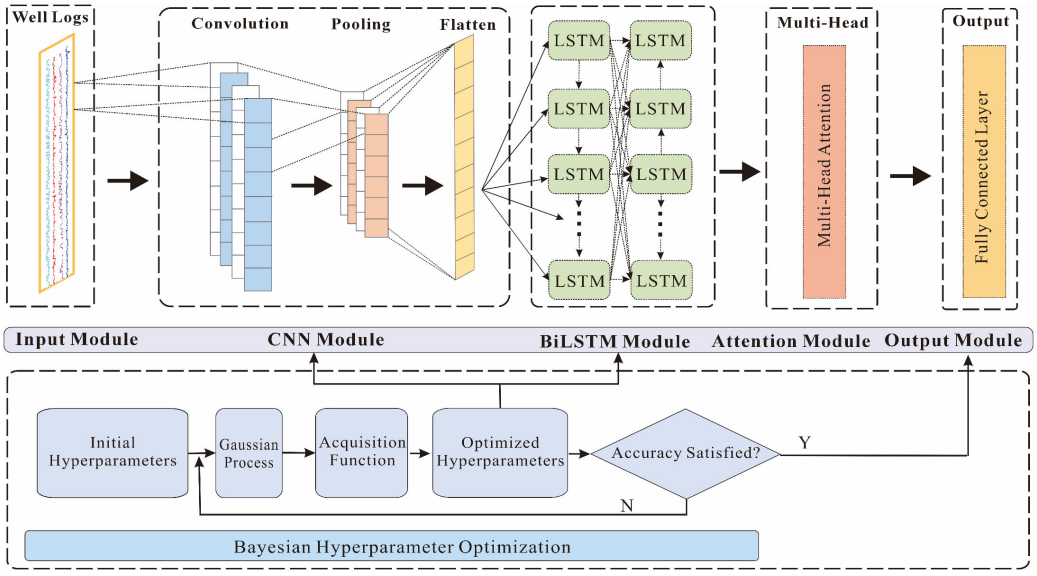


Figure 11. Network architecture for resistivity reconstruction.

4. Theoretical Basis for Water-Flooded Zone Identification Using Resistivity Reconstruction

4.1. Feature Variable Selection

Reconstructing original formation resistivity relies on logging measurements that provide information on lithology, electrical behavior, pore structure, and fluid occurrence. The choice of input logs is therefore critical because it influences both training stability and the model's ability to capture complex reservoir responses. Therefore, the following principles were considered during feature selection. First, sensitivity of physical response was considered by giving priority to logging curves that are sensitive to lithology, porosity, and fluid properties. Second, information complementarity was considered by selecting logging curves with complementary response mechanisms and limited information redundancy. Third, data completeness and reliability were considered to ensure that the selected curves have sufficient coverage and good measurement quality within the study intervals, thereby improving data stability and usability [30].

Based on their physical responses and data availability, five conventional logs were retained as model inputs: gamma ray (GR), photoelectric absorption cross section (PE), density (DEN), compensated neutron (CNL), and acoustic transit time (AC). Together, these measurements provide complementary information on lithology, mineral composition, porosity, pore-fluid conditions, and reservoir structure. Measured resistivity (R_t) was not included among the model inputs; it served as the prediction target for unflooded intervals and was subsequently used to calculate the resistivity attenuation ratio. SP was also not included in the selected input set.

(1) GR is primarily sensitive to shale content and lithological variation. Because clay-bound water influences the electrical response of the formation, GR provides useful information for accounting for shale-related effects on resistivity.
(2) PE is sensitive to the mineral composition of the rock matrix and can be used to distinguish different lithologies. Variations in mineral composition are associated with differences in electrical properties and therefore affect formation resistivity.
(3) DEN reflects the bulk density of the formation and can be used to characterize variations in porosity. Porosity controls the available pathways for electrical conduction and is therefore an important factor affecting formation resistivity.
(4) CNL is sensitive to the hydrogen index and can reflect changes in pore-fluid content. During water flooding, an increase in free water enhances the neutron response, making CNL useful for indicating fluid-related changes.
(5) AC responds sensitively to variations in formation elasticity and pore configuration.

To improve the effectiveness of the input features used by the neural network, correlation analysis was subsequently conducted to quantify the associations between individual logging variables and the prediction target. The correlation analysis of the logging data is presented in Figure 12. Pearson correlation coefficients were calculated to quantitatively evaluate the relationships between individual logging curves and the degree of water flooding, and parameters with relatively strong correlations were selected [31]. This analysis helps reduce feature redundancy while improving model training efficiency and prediction stability. Feature selection was conducted using the model-development data. The independent evaluation and additional validation wells were not used to determine the input-log combination.

4.2. Data Preprocessing

Prior to model input, the logging data were preprocessed to maintain data reliability and support stable training with better generalization. Accordingly, the original logging data

were systematically processed before model development. The preprocessing procedure mainly consisted of four steps: data cleaning and outlier treatment, sequence sample construction, dataset construction and splitting, and data normalization.

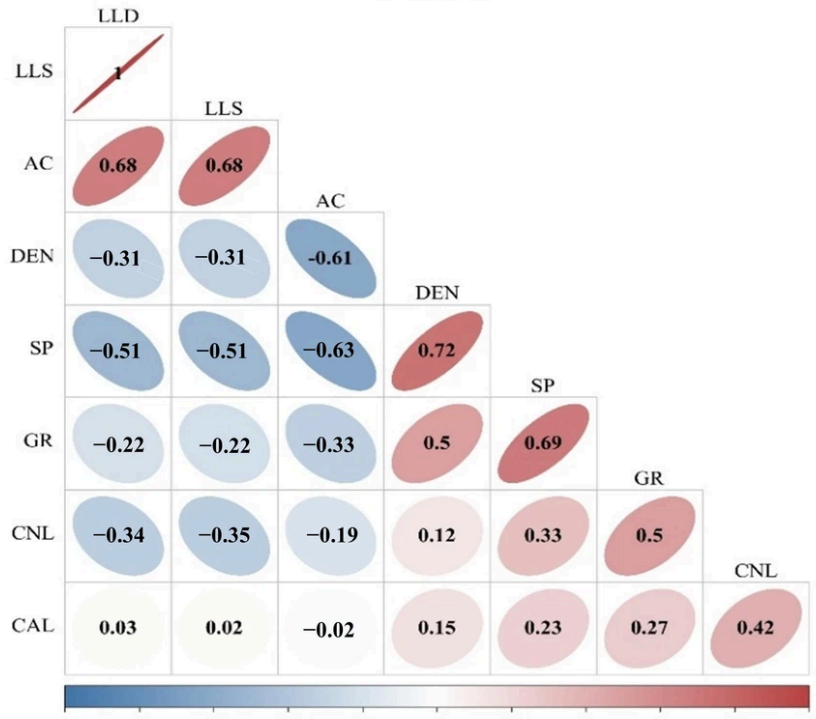


Figure 12. Correlation analysis of the logging data.

(1) Data Cleaning and Outlier Treatment

During well logging acquisition, variations in instrument operating conditions, complex downhole environments, and changes in borehole diameter may introduce abnormal responses into the original logging curves. These anomalies commonly appear as abrupt local changes, spike noise, or fluctuations that are inconsistent with geological trends. Such responses do not conform to the general continuity of formation properties along depth. If they are not properly identified and treated, they may distort the overall data distribution, reduce the stability of parameter learning during model training, and weaken model generalization, ultimately affecting the accuracy and reliability of original resistivity reconstruction. A local 3σ criterion was used for outlier detection. Within each sliding window, μ and σ were obtained from the local data distribution. Any observation beyond the range $(\mu - 3\sigma, \mu + 3\sigma)$ was flagged as anomalous according to Equation (15) and then treated as missing. The identified outliers and missing values were then reconstructed using locally weighted regression, or LOWESS, as described in Equations (16)–(20). This method fits a weighted regression model within a local neighborhood and assigns distance-dependent weights to nearby valid observations, allowing the logging curve to be reconstructed smoothly and continuously. Compared with simple median filtering or mean interpolation, LOWESS better retains the large-scale variation in logging curves and local responses around formation boundaries while limiting the effect of isolated anomalies. This preprocessing strategy removes abnormal noise while retaining the main electrical characteristics of the formation, thereby providing a stable and reliable data basis for subsequent reconstruction of the original formation resistivity.

$$\mu = \frac{1}{n}\sum_{i=1}^{n} x_i \tag{15}$$

$$\sigma = \sqrt{\frac{1}{n}\sum_{i=1}^{n}(x_i - \mu)^2} \tag{16}$$

$$|x_i - \mu| > 3\sigma \tag{17}$$

where x_i denotes the i-th logging value within the window, n gives the sample count within the current window, μ is the local mean, and σ is the local standard deviation.

A distance-based weighting function is then constructed so that observations closer to the target point receive larger weights during local regression, whereas more distant observations are assigned smaller weights.

$$w_i = \begin{cases} \left(1 - \left(\frac{d_i}{d_{\max}}\right)^3\right)^3, & d_i < d_{\max} \\ 0, & d_i \geq d_{\max} \end{cases} \tag{18}$$

A weighted least-squares fit is performed over the neighboring samples to obtain the local regression coefficients, which are subsequently used to estimate the value at the target location.

$$\min_{\beta_0,\beta_1} \sum_{i=1}^{n} w_i(y_i - (\beta_0 + \beta_1 x_i))^2 \tag{19}$$

$$\hat{y}(x_0) = \beta_0 + \beta_1 x_0 \tag{20}$$

Here, d_i denotes the separation between the target location, d_{max} is the largest distance within the selected neighborhood, and w_i is the weight assigned to the corresponding sample. β_0 and β_1 are obtained from the weighted least-squares solution of the local regression.

(2) Sequence Sample Construction

Well-log data are typical depth-dependent sequential data. Formation responses recorded at a given depth are often related to the lithology, reservoir petrophysical properties, and fluid characteristics of the adjacent intervals above and below. To make full use of these local vertical relationships during the training process, a sliding-window strategy was applied to transform individual logging points into continuous sequence samples, thereby satisfying the input requirements of the CNN and BiLSTM components. The sliding-window method is widely used for sequential data analysis and well-log prediction, particularly when strong local correlations exist along the sequence. In this study, a fixed-size window was shifted along the depth axis to capture local variations in the logging curves. Each extracted sequence was subsequently paired with its target value to form a training sample.

For well-log prediction, the sliding-window method is used to organize logging responses from multiple consecutive depth points into a single input sample, thereby explicitly incorporating vertical geological continuity. The sliding-window configuration is mainly controlled by two parameters: window size and stride. The former defines the depth range represented by a sample, whereas the latter specifies the shift between two consecutive windows. To avoid ambiguity in notation, the window half-width is denoted by N, the total window length by L, and the sliding step by S. Considering the strong depth-wise correlation of logging curves and the need to maintain continuity in the predicted profile, the stride was set to S = 1, meaning that the window moves downward by one sampling point at each step. This setting allows the model to capture detailed contextual information around each target depth and helps improve prediction accuracy and reliability. For each target depth, a continuous sequence centered on that point is extracted, including N sampling points above and N sampling points below. The total window length is therefore L = 2N + 1. The target associated with each training sequence is the measured formation resistivity at the corresponding central depth in an interval interpreted as unflooded. The

reference intervals were selected from wells identified as unflooded, and their measured resistivity values were used as the supervised learning targets. Accordingly, the supervised learning process establishes a mapping between the selected conventional logging responses and the measured resistivity characteristics of the reference unflooded reservoirs. When the trained model is applied to a water-flooded interval, its output is interpreted as an estimated unflooded reference resistivity rather than a directly measured historical pre-flooding resistivity. In this study, the symbol R_{t0} is retained to denote this model-estimated reference resistivity in the subsequent water-flooding analysis. In this way, each target point is associated with its local vertical geological context. Considering both prediction performance and computational efficiency, the window size was ultimately determined as 21 sampling points, with a half-window width of N = 10. The sliding-window procedure is illustrated in Figure 13.

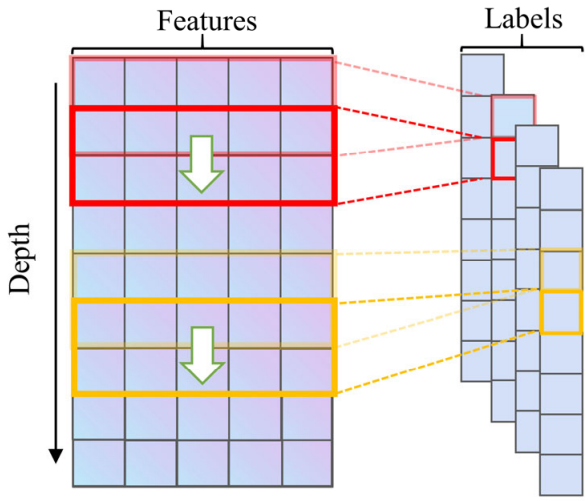


Figure 13. Schematic diagram of sliding window.

(3) Dataset Construction and Splitting

To avoid information leakage, the data partitions were established before the partition-specific preprocessing and sliding-window construction described below. Following well-level partitioning, sequence samples were constructed separately within the corresponding datasets to prevent overlap between model-development and independent-evaluation samples. Because the sliding-window method generates highly overlapping samples, adjacent samples are strongly correlated. A random split could therefore place nearly identical sequences in both model development and evaluation subsets, introducing information leakage and inflating the apparent generalization performance. To avoid this issue, the data were partitioned by well rather than by individual sample.

As summarized in Table 1, three unflooded wells and one water-flooded well were included in this study. Well A was used for model development, including training and internal validation. Well B was reserved for independent evaluation, while Well C provided additional cross-well validation. Well A was divided into training and validation subsets using continuous depth intervals, with the validation set used for hyperparameter optimization and early stopping. Wells B and C were excluded from model optimization and data augmentation. The trained model was subsequently applied to the water-flooded Well D as a separate application case. Wells A and B were selected because they contain reference unflooded intervals with the required input logs and measured resistivity. These two wells belong to the same reservoir system and target interval, with comparable depth ranges and logging responses, ensuring geological consistency between the development and independent evaluation datasets. No samples from the evaluation well were involved

in parameter learning. In addition, a representative water-flooded well was reserved as an external application case and excluded from both training and hyperparameter tuning. The model calibrated on the unflooded data was then used to reconstruct the original formation resistivity of this application well, and the reconstructed curve was compared with the measured resistivity to examine its suitability for water-flooded zone interpretation.

Table 1. Summary of the well-log datasets used in this study.

Well	Reservoir Condition	Depth Interval (m)	Raw Sampling Points	Valid Sequence Samples	Dataset Role
A	Unflooded	1020–1120	801	781	Model development
B	Unflooded	1000–1090	721	701	Independent evaluation
C	Unflooded	1030–1110	641	621	Additional cross-well validation
D	Water-flooded	1050–1110	481	461	Field application

Within the model-development well, the logging data were further divided into training and validation subsets using non-overlapping, continuous depth intervals. The dataset division was performed prior to sliding-window sampling, and sequence samples were independently generated within the corresponding subsets. Windows crossing the partition boundary were excluded to prevent overlap between the training and validation samples. The validation subset served as the basis for hyperparameter tuning and early stopping criteria. The independent evaluation well and the additional validation well were excluded from both model training and parameter adjustment.

(4) Data Normalization

Well-level partitioning limits the correlation between overlapping samples and provides a more robust evaluation of prediction performance on an independent well. After data cleaning, the logging variables were normalized because their units and numerical scales differ considerably. Direct use of the original values may cause large-magnitude features to exert excessive influence during optimization and disturb gradient-based learning. Therefore, Min-Max scaling was employed to transform all input variables into a unified range. This treatment reduces scale-related bias among the logging features and facilitates more stable and efficient model convergence [32].

$$x' = \frac{x - x_{\min}}{x_{\max} - x_{\min}} \tag{21}$$

where x is the original data value, $x_{\min}$ and $x_{\max}$ are the minimum and maximum values of the corresponding feature, respectively, and x' is the normalized value scaled to the range $[0, 1]$. The normalization parameters were determined only from the training subset. These scaling parameters were then directly applied to the validation, independent test, and additional validation datasets without recalculation. Thus, information from the held-out wells was not used to determine the normalization parameters.

4.3. Resistivity Reconstruction Results and Performance Analysis

After training, Well B was used as an independent test well, and reconstruction was performed within its unflooded intervals. The predicted resistivity was compared with the measured curve to examine how well each model reproduced the electrical response and depth-dependent variation in the formation. The CNN-BiLSTM-Attention was evaluated against CNN, BiLSTM, and CNN-BiLSTM baselines. Five logging curves were used as model inputs, including GR, AC, DEN, PE and CNL. These parameters characterize reservoir lithology, pore structure, and fluid properties from different perspectives. After

normalization, the five logging curves were used as input features for model prediction. In the reconstruction profiles, depth is plotted on the vertical axis and resistivity on the horizontal axis. Unflooded intervals in the independent test well were used to evaluate the ability of each model to reconstruct the original formation resistivity and reproduce its variation with depth.

The model configuration was optimized through Bayesian search over the main hyperparameters, including convolution kernel size, LSTM units, attention dimension, learning rate, and batch size. Mean squared error (MSE) was selected as the optimization criterion during model training, with Adam used for parameter optimization. The search ranges and selected values are summarized in Table 2. Early stopping was applied by monitoring the validation loss after each training epoch. The training process was stopped if no further reduction in validation loss was observed over 10 successive epochs.

Table 2. Search ranges and optimal settings of model hyperparameters.

Model Hyperparameter	Search Range	Optimal Value
Convolution kernel size	3~7	5
Number of convolution filters	16~64	32
Number of LSTM units	64~256	128
Number of LSTM layers	1, 2	2
Attention dimension	32~128	64
Dropout rate	0.1~0.5	0.3
Learning rate	10^{-4}~10^{-2}	0.0005
Batch size	32~128	64
Number of training epochs	50~200	100

The experimental results show clear differences in the performance of the four models for resistivity R_t curve reconstruction. As illustrated in Figure 14, CNN captures local variations in the logging responses but shows limited ability to follow the overall resistivity trend, resulting in larger deviations in several intervals. The BiLSTM model uses bidirectional recurrent structures to capture sequential information and performs better in representing vertical variations, leading to greater consistency between the reconstructed and measured curves in terms of their overall trends. CNN-BiLSTM further improves local detail representation by combining convolution-based feature extraction with bidirectional sequence learning, leading to smoother and more accurate reconstruction. The CNN-BiLSTM-Attention model delivers the most consistent performance and tracks resistivity variations more closely across different depths. This improvement indicates that the attention module helps emphasize informative representations and enhances the accuracy of resistivity reconstruction.

To reduce the subjectivity associated with visual comparison of curve shapes alone, scatterplots between the reconstructed and measured resistivity values were further constructed to evaluate their correlation and degree of dispersion. Figure 15 shows that data points generated by all models are relatively concentrated in the low and moderate resistivity ranges, with limited scatter, indicating relatively high prediction accuracy in these intervals. In the high-resistivity range, however, greater dispersion is observed for some models, with some data points showing noticeable deviations from the 1:1 reference line. This indicates that the models exhibit reduced fitting performance when predicting extreme resistivity values, which may be related to the smaller number of high-resistivity samples and the stronger reservoir heterogeneity in these intervals. To quantify these differences, a further error analysis was performed for the proposed model under different measured resistivity intervals.

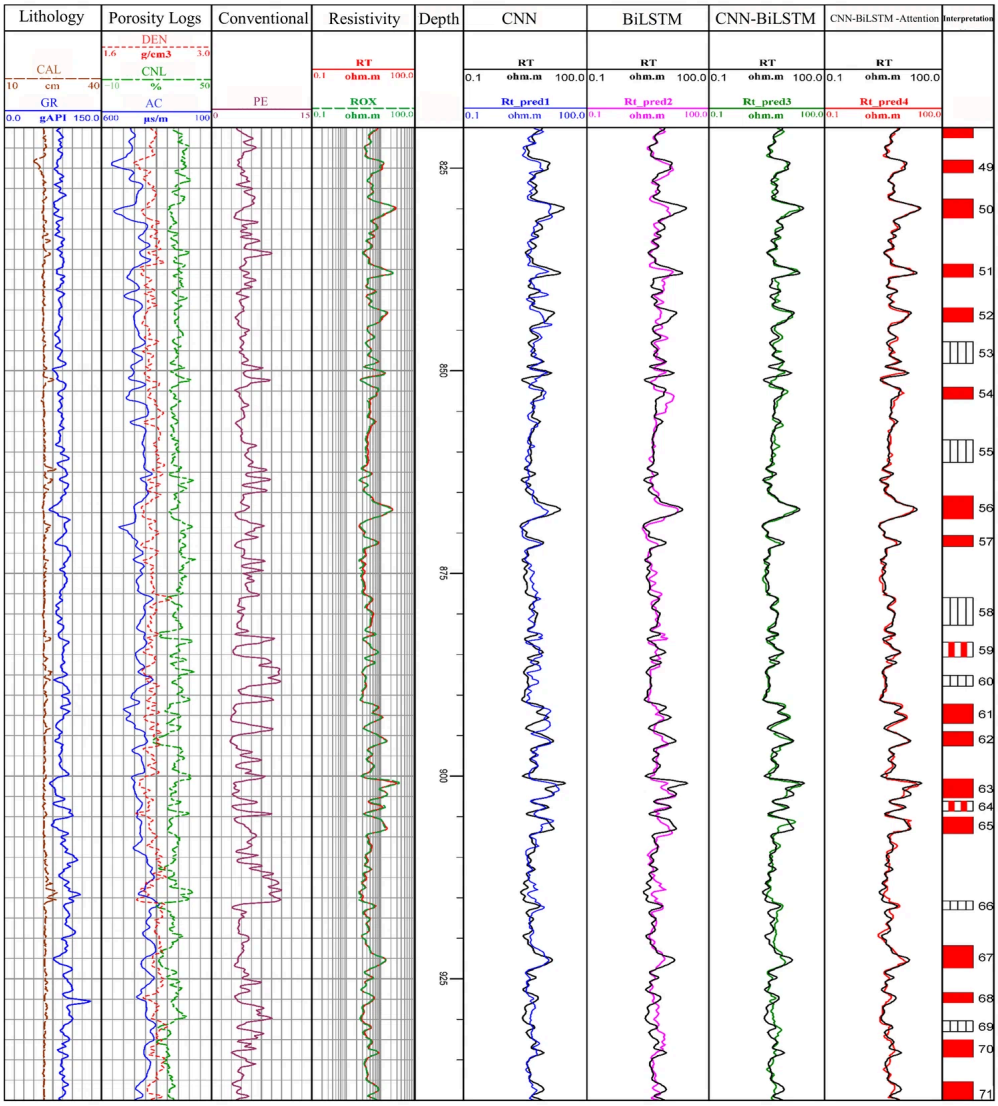


Figure 14. Resistivity reconstruction results of different algorithms for Well B.

Model performance was further assessed using four quantitative indicators: root mean square error (RMSE), mean absolute error (MAE), mean absolute percentage error (MAPE), together with the coefficient of determination R^2. These metrics were used to comprehensively assess the agreement between the reconstructed and measured resistivity values. By combining multiple evaluation criteria, the reconstruction accuracy of each model and its ability to reproduce the variation trend of resistivity can be assessed more objectively.

$$RMSE = \frac{1}{n}\sqrt{\sum_{i=1}^{n}(\hat{y}_i - y_i)^2} \tag{22}$$

$$MAE = \frac{1}{n}\sum_{i=1}^{n}|\hat{y}_i - y_i| \tag{23}$$

$$MAPE = \frac{1}{n}\sum_{i=1}^{n}\left|\frac{\hat{y}_i - y_i}{y_i}\right| \times 100\% \tag{24}$$

$$R^2 = \frac{\sum_{i=1}^{M}(\hat{y}_i - \overline{y})^2}{\sum_{i=1}^{M}(y_i - \overline{y})^2} \tag{25}$$

To further examine the performance of the proposed framework, conventional machine-learning models and different ablation configurations were introduced for comparison. All models were tested under an identical data partition, while hyperparameter optimization was performed using the validation subset from the model-development dataset. To evaluate the stability of model performance, the proposed network was trained repeatedly using different random seeds. Table 3 summarizes the evaluation metrics obtained by the different models for resistivity reconstruction. Hybrid model yields the smallest RMSE, MAE, and MAPE, together with the largest R^2 among the evaluated models. This performance demonstrates stronger error control and closer fitting than the comparison models, enabling more accurate reproduction of resistivity variations.

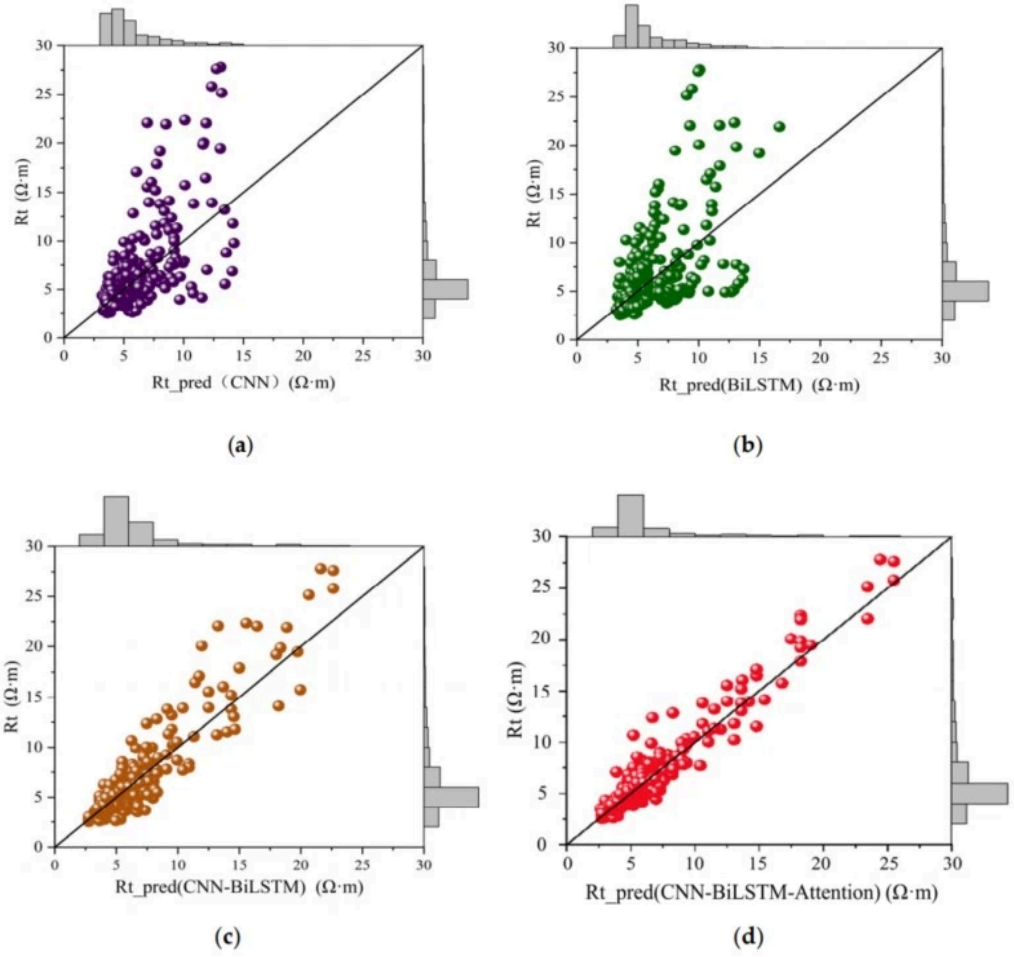


Figure 15. Comparison between reconstructed and measured resistivity values for the four algorithms. (**a**) CNN (**b**) BiLSTM (**c**) CNN-BiLSTM (**d**) CNN-BiLSTM-Attention.

Compared with conventional machine-learning approaches, including RF and XGBoost, the deep learning models achieved improved prediction accuracy, indicating that sequential feature extraction is beneficial for capturing nonlinear relationships between logging responses and original formation resistivity. Both BiLSTM and CNN-BiLSTM are capable of reconstructing well-log curves, but CNN-BiLSTM performs more favorably in intervals with complex responses and strong local fluctuations. After incorporating attention, the model gains a stronger ability to represent detailed logging patterns and long-range dependencies along the sequence. By emphasizing informative representations and suppressing redundant information, the attention module further improves reconstruction accuracy on the evaluated well. The ablation results further indicate that data augmentation, window length, and input-log selection affect reconstruction performance.

Among the evaluated settings, the complete model with a window length of 21 achieved lower prediction errors, supporting the adopted configuration.

Given the greater prediction dispersion observed in the high-resistivity range in Figure 15, the reconstruction errors were further evaluated across different measured-resistivity intervals, as summarized in Table 4. All experiments were conducted using the same random seed to ensure a fair comparison among different configurations.

Table 3. Comparison of evaluation metrics for resistivity reconstruction using different models and ablation settings.

Model	RMSE	MAE	MAPE (%)	R^2
RF	2.1863 ± 0.053	1.5423 ± 0.042	18.76 ± 1.13	0.7125 ± 0.028
XGBoost	1.9841 ± 0.059	1.3262 ± 0.036	16.45 ± 1.31	0.7581 ± 0.026
CNN	1.7434 ± 0.062	1.3894 ± 0.045	19.12 ± 1.26	0.6463 ± 0.018
BiLSTM	1.7044 ± 0.058	1.3116 ± 0.039	18.82 ± 1.14	0.6856 ± 0.021
CNN-BiLSTM	1.3984 ± 0.041	0.8095 ± 0.032	13.82 ± 0.86	0.8361 ± 0.014
CNN-BiLSTM-Attention (L = 21)	1.1286 ± 0.035	0.6136 ± 0.027	8.46 ± 0.51	0.9186 ± 0.012
without augmentation	1.2834	0.7127	10.14	0.8947
L = 11	1.2157	0.6689	9.24	0.9056
L = 31	1.1793	0.6418	8.91	0.9113
without CNL	1.2038	0.6576	9.08	0.9074

Table 4. Stratified reconstruction errors of the CNN-BiLSTM-Attention model across different resistivity ranges.

Measured Resistivity (Ω·m)	Count	RMSE	MAE
$R_t < 5$	390	0.5512	0.3215
$5 \leq R_t < 10$	250	1.1023	0.7286
$R_t \geq 10$	61	2.7776	2.0098
Overall	701	1.1286	0.6136

The stratified results indicate that reconstruction errors increase with resistivity, particularly in the high-resistivity range. This finding is consistent with the dispersion observed in Figure 15 and suggests reduced prediction reliability in high-resistivity intervals.

To further assess cross-well predictive performance, the trained model was independently evaluated on Well C without further training or hyperparameter adjustment. The resulting RMSE, MAE, MAPE, and R^2 were 1.2843, 0.7218, 10.27%, and 0.8821, respectively. This additional evaluation provides further evidence of the model's predictive capability within the investigated reservoir setting.

The attention scores provide a visualization of the relative weighting of learned feature representations generated by the network. Figure 16 presents the averaged attention scores and their standard deviations across the evaluation samples. The differences among the learned feature representations reflect model-dependent weighting patterns rather than direct measurements of physical feature importance. The attention scores vary among different learned representations, indicating that the model dynamically emphasizes informative features during reconstruction. This adaptive weighting mechanism enables the network to focus on informative latent representations during resistivity reconstruction. Therefore, the attention analysis is used as a qualitative interpretation of model behavior rather than a quantitative measurement of logging-variable contribution.

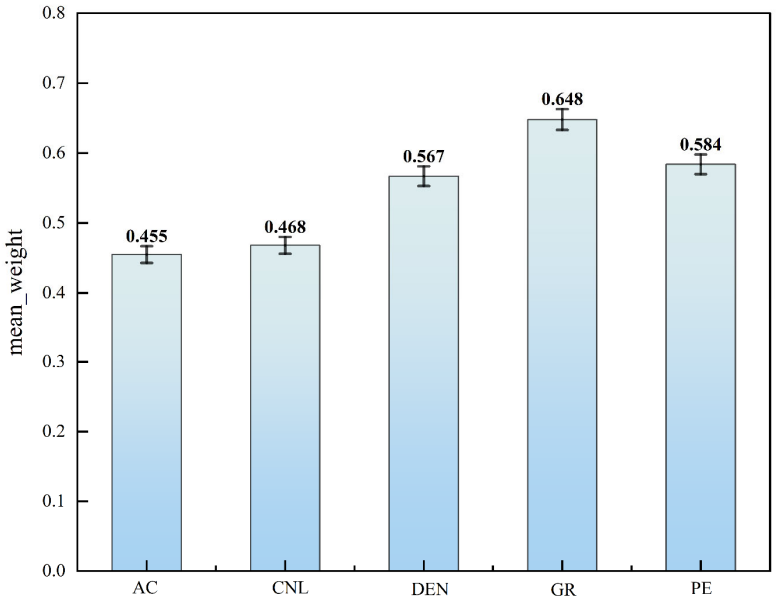


Figure 16. Normalized attention scores of learned feature representations.

5. Practical Application and Performance Analysis of Water-Flooded Zone Identification Based on Resistivity Reconstruction

Recent machine-learning methods have been increasingly utilized for water-flooded layer identification, offering additional data-driven approaches for reservoir interpretation [33]. To examine the applicability of the proposed reconstruction approach to water-flooded zone interpretation, Well D was selected as an application case. The trained model was applied to the conventional logging data from this well to estimate its resistivity under the reference unflooded conditions represented by the training data. The estimated reference resistivity was subsequently compared with the measured resistivity to investigate the electrical differences associated with reservoir water flooding. It should be noted that the reconstructed reference curve is a model-based estimate rather than a direct measurement of the historical pre-flooding resistivity.

To establish the reference categories for water-flooding evaluation, the investigated intervals were classified into four groups: oil-bearing, weak, moderate, and strong water-flooded intervals. The reference labels were established based on formation-test records, including the corresponding fluid-production characteristics and test water cut. Reference labels were assigned at the formation-test interval level, and the corresponding logging samples inherited the label of their respective tested intervals. Thus, the reported sample counts represent logging observations rather than independent formation tests. The classification criteria and sample distributions for the four categories are summarized in Table 5.

Table 5. Reference water-flooding categories established from formation-test data.

Reference Category	Test Size	Classification Criterion
Oil-bearing	30	Predominantly oil production, with a test water cut of 0–5%
Weakly water-flooded	32	Oil and water production, with a test water cut of >5–30%
Moderately water-flooded	31	Oil and water production, with a test water cut of >30–70%
Strongly water-flooded	32	Water-dominated production, with a test water cut of >70–100%

The reference labels were established independently of the reconstructed resistivity and the attenuation ratio M. Neither M nor the measured resistivity used in its calculation was employed to determine the reference categories. This separation was maintained to avoid

circularity between reference-label assignment and classification evaluation. Formation-test data were used to establish the reference categories, whereas the reconstructed-to-measured resistivity contrast was used to characterize their logging responses and develop the subsequent classification scheme.

As shown by the comparison of resistivity curves in Figure 17, within the depth interval of 1059 to 1062 m, the measured resistivity curve shifts markedly toward lower values, whereas the reconstructed resistivity remains at a relatively high level. The clear separation between the two curves indicates enhanced electrical conductivity of the reservoir and suggests an increase in the proportion of conductive water within the pore space. The observed resistivity contrast is consistent with the logging response expected for a weakly water-flooded interval. At approximately 1064 to 1067 m, the measured resistivity decreases further, while the reconstructed resistivity remains relatively high, resulting in a substantially greater difference between the two curves. This indicates a more pronounced influence of water invasion, with a marked increase in pore-water content and a corresponding change in the electrical response of the reservoir. The larger resistivity contrast suggests a logging response characteristic of stronger water flooding. Within the 1075 to 1080 m interval, a distinct difference between the reconstructed and measured resistivity curves can also be observed. Intervals showing relatively large differences are interpreted as moderately water-flooded zones, whereas those with smaller differences are characterized as weakly water-flooded zones. The degree of separation between the reconstructed and measured resistivity curves therefore provides a direct indication of changes in reservoir electrical properties and can effectively reflect both the location and intensity of water flooding. From a physical perspective, before water invasion occurs, the pore space is dominated by the oil phase, resulting in relatively weak formation conductivity and comparatively high resistivity. As injected water or formation water enters the reservoir, the proportion of conductive water in the pore space gradually increases, which enhances formation conductivity and leads to a pronounced decrease in the measured resistivity. Therefore, reconstructing the original resistivity response of the reservoir and comparing it with the measured resistivity provides an effective approach for identifying water-flooded intervals and evaluating the degree of water flooding.

Analysis of the other logging curves shows that the acoustic transit time also exhibits a pronounced increase within the water-flooded interval. This response suggests that the pore structure of the formation may have changed. Increased water saturation may reduce the effective acoustic velocity through the formation, resulting in a longer acoustic transit time. This variation corresponds well with the decrease in resistivity and constitutes a characteristic logging response of a water-flooded zone. More importantly, no oil flow was observed during formation testing of this interval, which is highly consistent with the well-log interpretation results. This agreement provides supporting evidence for the water-flooding interpretation of the investigated interval. Nevertheless, the formation-test result represents interval-specific evidence and should not be regarded as independent validation of all reference categories used in the subsequent classification analysis.

To further improve the interpretability of the reconstruction results for engineering applications, the reconstructed original formation resistivity R_{t0} was compared with the measured resistivity obtained from conventional logging. On this basis, a physically meaningful parameter, termed the resistivity attenuation ratio M, was introduced to quantify the degree of change in formation electrical properties relative to the original reservoir state. The resistivity attenuation ratio is calculated as follows:

$$\mathrm{M} = \frac{R_{t0} - R_t}{R_t} \tag{26}$$

where R_{t0} and R_t denote the reconstructed original formation resistivity and the measured formation resistivity obtained from well logging, respectively, in Ω·m. M is the resistivity attenuation ratio, which represents the relative decrease in resistivity caused by water flooding or other related factors. The M value represents the relative difference between the estimated reference resistivity and the measured resistivity, normalized by the measured resistivity. In practical calculations, abnormal or extremely small R_t values were carefully examined before calculating M to reduce potential numerical instability caused by a denominator approaching zero. Theoretically, for an unflooded reservoir, R_{t0} and R_t are close to each other, and M approaches zero. As the degree of water flooding increases, the increase in water saturation causes a more pronounced decrease in R_t, resulting in a larger M value. In practical calculation, all investigated samples exhibited positive measured resistivity values, and no extremely low R_t values causing denominator instability were observed. Therefore, no artificial lower-bound correction was applied to R_t, and the calculated M values were directly used for subsequent crossplot analysis and water-flooding interpretation. However, M represents a relative difference between the estimated reference resistivity and the measured resistivity, rather than a direct measurement of water-flooding intensity. It may also be influenced by lithology, pore structure, formation-water salinity, mud invasion, and logging conditions. Therefore, M is regarded as a supporting parameter for identifying water-flooded zones. The indicative M ranges were determined from the distributions of formation-test-labeled calibration samples and the corresponding crossplot boundaries. These ranges describe the predominant responses of each category rather than independent, rigid classification thresholds; overlapping samples were evaluated using the integrated M+GR+AC scheme.

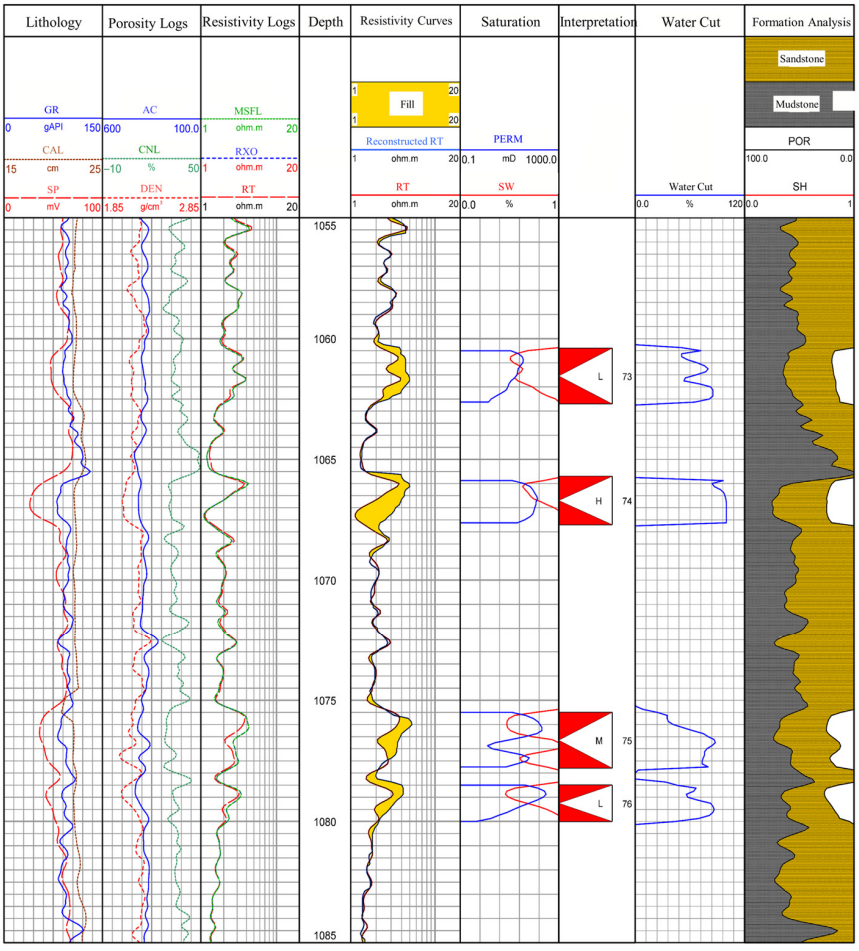


Figure 17. Identification of water-flooded zones based on resistivity reconstruction.

The distribution of M shows a certain degree of overlap between oil-bearing zones and weakly water-flooded zones in the low-value range, mainly at M ≈ 0.05~0.20. This indicates that a single parameter is insufficient to effectively distinguish these two reservoir types. The main reason is that weakly water-flooded zones are only slightly affected by water displacement, resulting in limited resistivity changes and electrical responses similar to those of the original oil-bearing zones.

To reduce interpretation uncertainty and further improve the reliability of water-flooding identification, additional logging parameters that characterize reservoir lithology and petrophysical properties are required for integrated analysis. Gamma ray (GR) reflects variations in shale content and lithology, whereas acoustic transit time (AC) is relatively sensitive to reservoir pore structure and petrophysical properties. Therefore, GR mainly offers lithological information to assist the interpretation of M variations, rather than directly reflecting the severity of water flooding. M-GR and M-AC crossplots integrate resistivity attenuation with lithological and petrophysical responses, allowing clearer discrimination among reservoirs with different water-flooding intensities and improving interpretation reliability. The independent unflooded evaluation wells were not used to establish or adjust the water-flooding classification thresholds.

As shown in the GR-M crossplot in Figure 18, samples with different fluid characteristics exhibit relatively distinct distribution patterns along the resistivity attenuation ratio M. Based on the distribution characteristics of M values and the separation of different water-flooded categories in the labeled reservoir samples, the corresponding classification thresholds were determined. Oil-bearing samples are mainly concentrated in the low-value range of M ≈ 0~0.05, indicating that these intervals are essentially unaffected by water flooding and that the measured resistivity is nearly identical to the original formation resistivity. Weakly water-flooded samples are mainly distributed within M ≈ 0.05~0.2, whereas moderately water-flooded samples are concentrated in the range of M ≈ 0.2~0.45. These distributions indicate that the resistivity attenuation ratio gradually increases with increasing water-flooding intensity. Strongly water-flooded samples are mainly distributed in the high-value region of M > 0.5, indicating a significant enhancement of water saturation within the formation and a consequent reduction in resistivity. In terms of GR, the separation among different water-flooding categories is relatively limited, indicating that GR primarily reflects lithological variations and has limited sensitivity to the degree of water flooding. Therefore, GR mainly provides a lithological constraint, while M remains the principal indicator of flooding-related resistivity contrast in this crossplot.

In the AC-M crossplot shown in Figure 19, samples corresponding to different degrees of water flooding also exhibit distinct zonation characteristics. Oil-bearing samples are mainly concentrated within the region of AC ≈ 250~310 μs/m and M ≈ 0~0.05, characterized by a low resistivity attenuation ratio. Strongly water-flooded samples are mainly distributed in the high-M region and generally exhibit larger AC values. Because acoustic transit time is closely related to reservoir pore structure and petrophysical properties, it can provide information on reservoir quality in addition to resistivity variations. Therefore, jointly analyzing the resistivity attenuation ratio M and AC can enhance the discrimination of reservoirs experiencing different flooding levels by incorporating the effects of reservoir petrophysical properties.

To further quantitatively evaluate the ability of different parameter combinations to identify the degree of water flooding, three classification schemes, namely *M+GR*, *M+AC*, and the integrated *M+GR+AC* scheme, were used to classify oil-bearing and water-flooded intervals at weak, moderate, and strong levels.

To ensure an independent evaluation, the formation-test-labeled samples were separated into calibration and independent test subsets according to formation-test intervals. All

logging samples associated with the same tested interval were assigned to the same subset. The calibration and test sets comprised 180 and 125 logging samples from 12 and 8 separate formation-test intervals, respectively. The test subset consisted of 30 oil-bearing samples, 32 weak-flooding samples, 31 moderate-flooding samples, and 32 strong-flooding samples. The classification boundaries were established exclusively using the calibration set and were subsequently applied to the held-out test set without further adjustment. The M+GR and M+AC schemes employed decision boundaries in their respective two-dimensional crossplot spaces. For the integrated M+GR+AC scheme, the two classification results were first compared. Concordant assignments were retained, whereas discordant assignments were resolved according to the minimum normalized distance to the class centroids in the three-parameter space. The classification results were compared with the four reference categories defined in Table 5. The sample counts and the sources of the reference labels were kept consistent across the classification schemes. The resulting classifications were assessed with confusion matrices (Figure 20). Correct assignments appear along the main diagonal, whereas off-diagonal entries reflect classification errors between categories. Accuracy, precision, and recall were further calculated to compare the overall performance of the three schemes.

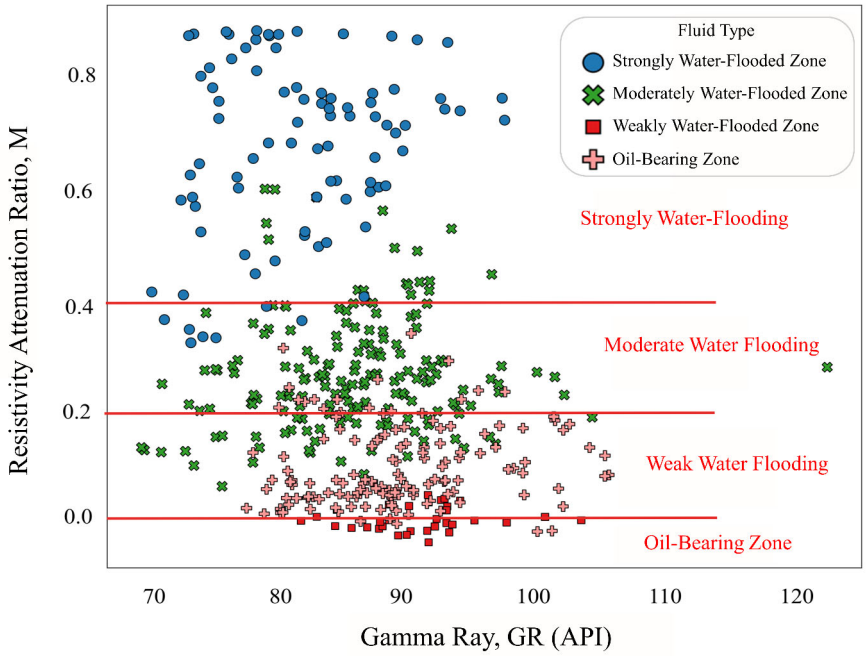


Figure 18. M-GR crossplot and classification boundaries established using the calibration set.

As shown in Figure 20, all three schemes achieve good classification performance, while the integrated *M+GR+AC* scheme provides the best overall discrimination among different water-flooding categories, with most misclassifications occurring between adjacent flooding levels. This result is consistent with the preceding crossplot analysis. The results demonstrate that integrating the original formation resistivity reconstructed by deep learning with conventional logging parameters can further improve the reliability of water-flooded zone identification and provide an effective basis for remaining-oil evaluation and subsequent reservoir development adjustment.

Table 6 summarizes the class-specific performance of the three classification schemes. The integrated M+GR+AC scheme achieved an overall accuracy of 93.6%, compared with 90.4% and 92.0% for the M+GR and M+AC schemes, respectively. The integrated scheme also showed improved F1-scores for weakly and moderately water-flooded intervals.

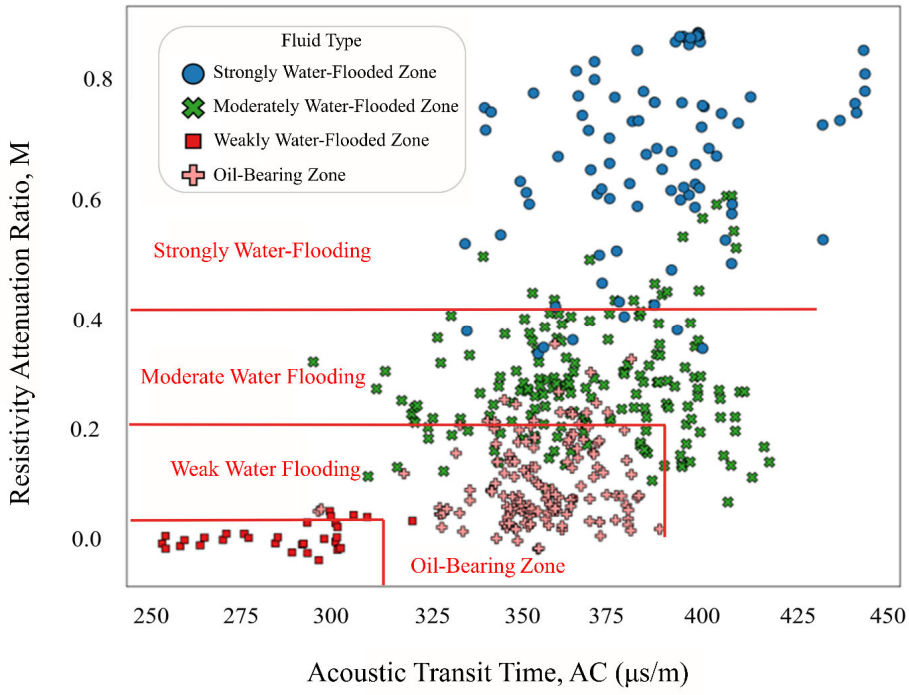


Figure 19. M-AC crossplot and classification boundaries established using the calibration set.

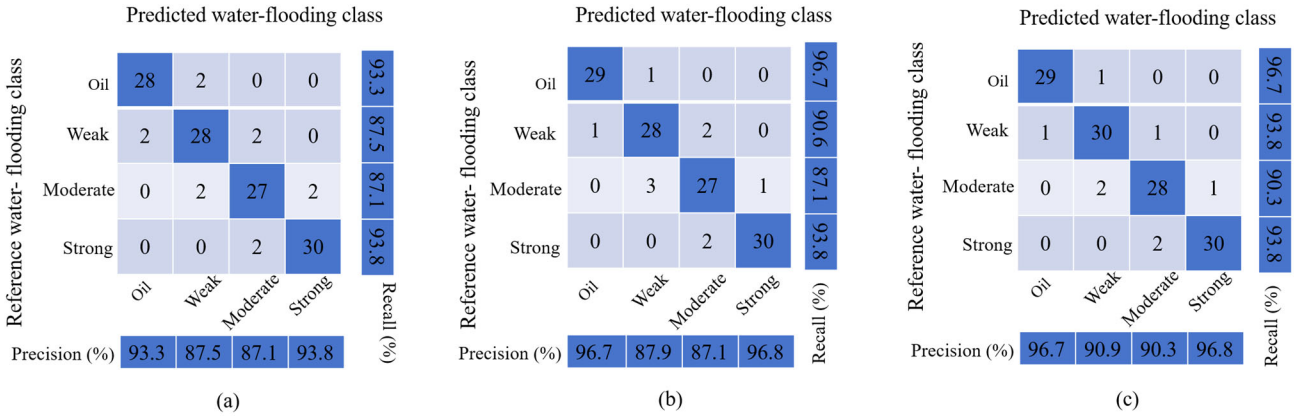


Figure 20. Confusion matrices of water-flooding classification using three schemes: (**a**) M+GR, (**b**) M+AC, and (**c**) integrated M+GR+AC.

Table 6. Class-specific performance of the three classification schemes.

Reference Class	*M+GR*	*M+AC*	*M+GR+AC*
Oil-bearing	93.3/93.3/93.3	96.7/96.7/96.7	96.7/96.7/96.7
Weakly water-flooded	87.5/87.5/87.5	87.9/90.6/89.2	90.9/93.8/92.3
Moderately water-flooded	87.1/87.1/87.1	87.1/87.1/87.1	90.3/90.3/90.3
Strongly water-flooded	93.8/93.8/93.8	96.8/93.8/95.2	96.8/93.8/95.2
Overall accuracy (%)	90.4	92.0	93.6

Note: Class-specific values are presented as Precision/Recall/F1-score (%).

To evaluate the added value of reconstructed reference resistivity, the M+GR+AC scheme was compared with the conventional Rt+GR+AC scheme using the same evaluation protocol. The reconstruction-assisted scheme achieved an accuracy of 93.6%, compared with 86.4% for the conventional scheme, representing an improvement of 7.2 percentage points.

6. Conclusions

Based on the observed logging responses, this study examined several approaches for water-flooded zone interpretation in the target reservoir. This study developed a reconstruction-assisted workflow for water-flooded zone identification using conventional well logs and estimated unflooded reference resistivity. The major conclusions obtained from this study are summarized below.

(1) The CNN-BiLSTM-Attention model was trained using GR, PE, DEN, CNL, and AC as inputs and measured resistivity from unflooded intervals as the prediction target. On the independent evaluation well, the model obtained RMSE, MAE, MAPE, and R^2 values of 1.1286 Ω·m, 0.6136 Ω·m, 8.46%, and 0.9186, respectively. Additional independent-well evaluation further examined its cross-well predictive performance.

(2) In complex heterogeneous reservoirs, conventional log interpretation may not fully capture the actual electrical behavior of the formation. To overcome this limitation, a deep learning approach was adopted to estimate the original formation resistivity from conventional logging responses. The trained network learns nonlinear relationships among the input logs to estimate an unflooded reference resistivity for the investigated reservoir. Comparison between the reconstructed and measured resistivity provides an auxiliary indicator water-flooding effects. On this basis, the resistivity attenuation ratio M was introduced and combined with GR and AC in crossplot analysis to distinguish different flooding levels. The integrated M+GR+AC scheme achieved a classification accuracy of 93.6%. The proposed workflow provides a reconstruction-assisted approach for water-flooding interpretation in the investigated reservoir. Its broader applicability to remaining-oil evaluation and reservoir-development decisions requires further validation using additional water-flooded wells and independent production data.

Although the additional independent-well validation provides further evidence of the model's predictive capability, its generalization across different geological settings requires further evaluation using larger multi-well datasets.

Author Contributions: Conceptualization, H.B. and K.L.; methodology, K.L. and Z.L.; software, K.L.; validation, K.L.; data curation, K.L., Q.M. and J.J.; writing—original draft preparation, K.L.; writing—review and editing, H.B. and F.W.; supervision, H.B. All authors have read and agreed to the published version of the manuscript.

Funding: This study was supported by the National Natural Science Foundation of China (No. 42304143), the National Key Research and Development Program Project (No. 2022YFC2904301) and the Shaanxi Provincial Natural Science Foundation (No. 2025JC-YBMS-312).

Data Availability Statement: Data will be made available on request from the corresponding author.

Conflicts of Interest: Authors Huiyuan Bian and Kun Li were employed by the College of Geology and Environment, Xi'an University of Science and Technology, Xi'an 710054, China. Authors Zhibin Lv, Qing Miao, and Jiantuan Jia were employed by the Qaidam Comprehensive Geological and Mineral Exploration Institute of Qinghai Province, Golmud 816099, China, and the Qinghai Provincial Key Laboratory of Salt Lake Resource Exploration and Research in Qaidam Basin, Golmud 816099, China. Author Fei Wang was employed by the College of Geology Engineering and Geomatics, Chang'an University, Xi'an 710054, China. The authors declare no conflicts of interest.

References

1. He, W.-Y.; Wu, Y.-D.; Feng, L.-X.; Li, C.-X.; Wan, J.-B.; Ni, G.-H. Research on the Mechanism of Complex Water-Flooded Layers and Well Logging Evaluation Methods in the M Oilfield. *Appl. Geophys.* **2025**, *22*, 1042–1057. [CrossRef]
2. Xu, W.; Zhang, Z.; Nie, X.; Zhang, Y.; Zeng, W.; Zhu, Z. A New Method for Identifying Water-Flooded Layers in Low-Resistivity Reservoirs. *J. Geophys. Eng.* **2026**, *23*, 501–516. [CrossRef]

3. Liu, B.; Peng, J.; Li, D.; Gao, D.; Jiang, Y.; Tan, C.; Zhu, Y. Water-flooded zone identification for Ordos Yan9 reservoir using conventional logs. *Sci. Rep.* **2026**. [CrossRef]
4. Bian, H.; Ji, J.; Zhang, H.; Fang, C.; Li, K.; Ma, Y.; Li, Y.; Wang, F. Logging Curve Reconstruction Method Based on CNN-BiLSTM With Integrated Attention Mechanism. *IEEE Geosci. Remote Sens. Lett.* **2025**, *22*, 1–5. [CrossRef]
5. Jiang, Z.; Fu, J.; Li, G.; Mao, Z.; Zhao, P. Using Resistivity Data to Study the Waterflooding Process: A Case Study in Tight Sandstone Reservoirs of the Ordos Basin, China. *Geophysics* **2021**, *86*, B55–B65. [CrossRef]
6. Bian, H.; Zhou, J.; Xu, Y.; Chen, Y.; Wang, W.; Wu, Y.; Ji, J. Intelligent Classification of Coal Body Structure in Logging Based on Wavelet Transform and BO-CNN-TransKAN Model. *Lithosphere* **2025**, *2025*, lithosphere_2025_108. [CrossRef]
7. Agga, A.; Abbou, A.; Labbadi, M.; El Houm, Y.; Ou Ali, I.H. CNN-LSTM: An efficient hybrid deep learning architecture for predicting short-term photovoltaic power production. *Electr. Power Syst. Res.* **2022**, *208*, 107908. [CrossRef]
8. Simoes, V.; Maniar, H.; Abubakar, A.; Zhao, T. Comparative Study of Machine-Learning-Based Methods for Log Prediction. *Petrophysics* **2023**, *64*, 192–212. [CrossRef]
9. Zhou, W.; Zhao, H.; Li, X.; Qi, Z.; Lai, F.; Yi, J. Missing Well Logs Reconstruction Based on Cascaded Bidirectional Long Short-Term Memory Network. *Expert. Syst. Appl.* **2025**, *259*, 125270. [CrossRef]
10. Gong, A.; Zhang, L.; Sun, Y.; Zhang, Y. Transformer–Kolmogorov–Arnold network for high-fidelity resistivity reconstruction toward fluid characterization. *Phys. Fluids* **2025**, *37*, 126608. [CrossRef]
11. Zhao, F.; Huang, W.; Zhao, Z.; Gong, W.; Wang, H.; Zhu, L.; Wang, W.; Bai, R.; Zhu, Y. Reconstruction of Well Logging Based on Adversarial Autoencoders and Transformers. *SPE J.* **2025**, *30*, 5177–5188. [CrossRef]
12. Liu, Z.; Wu, Z.; Zhao, X.; Zhao, Y. Prediction and Application of 0.2 m Resistivity Logging Curves Based on Extreme Gradient Boosting. *Processes* **2025**, *13*, 2741. [CrossRef]
13. Ge, X.; Ishag, M.; Li, H.; Liu, J.; Qu, C.; Mohamed, B. A Hybrid Inversion Algorithm to Obtain the Resistivity of the Uninvaded Zone Based on the Array Induction Log. *Comput. Geosci.* **2025**, *194*, 105766. [CrossRef]
14. Sheng, X.; Shen, J.; Shen, Y.; Zhu, L.; Zang, D. Measurement of formation conductivity through-casing using a TEM method. *J. Geophys. Eng.* **2019**, *16*, 439–450. [CrossRef]
15. Bian, H.; Ji, J.; Duan, C.; Zhou, J.; Li, K.; Ma, Y. Coal body structure identification method based on Bayesian-optimized CNN-BiLSTM-Attention. *Coal Geol. Explor.* **2025**, *53*, 34–43. [CrossRef]
16. Guo, H.; Liao, W.; Zhao, B.; Cheng, X.; Wang, K. Geology-Constrained Time Series Generative Adversarial Network for Well Log Curve Reconstruction. *Appl. Sci.* **2026**, *16*, 3421. [CrossRef]
17. Luo, P.; Jiang, J.; Wei, F.; Yang, B.; Ren, L.; Zhou, Y. Resistivity Restoration Using Spiking Neural Networks for Water-Flooded Zone Interpretation in High Water-Cut Sandstone Reservoirs. *Energy Geosci.* **2026**, *7*, 100523. [CrossRef]
18. Zou, Q.; Chen, Z.; Zhan, J.; Chen, C.; Gao, S.; Kong, F.; Xia, X. Morphological Evolution and Flow Conduction Characteristics of Fracture Channels in Fractured Sandstone under Cyclic Loading and Unloading. *Int. J. Min. Sci. Technol.* **2023**, *33*, 1527–1540. [CrossRef]
19. Tian, Y.; Xu, Z. Application of Deep Learning for Porosity Prediction in Tight Sandstone Reservoirs: A Case Study of Blocks Su14 and Su36. *J. Appl. Geophys.* **2025**, *243*, 105987. [CrossRef]
20. Fan, X.; Meng, F.; Deng, J.; Semnani, A.; Zhao, P.; Zhang, Q. Transformative Reconstruction of Missing Acoustic Well Logs Using Multi-Head Self-Attention BiRNNs. *Geoenergy Sci. Eng.* **2025**, *245*, 213513. [CrossRef]
21. Ma, T.; Xiang, G.; Shi, Y.; Liu, Y. Horizontal in Situ Stresses Prediction Using a CNN-BiLSTM-Attention Hybrid Neural Network. *Geomech. Geophys. Geo-Energ. Geo-Resour.* **2022**, *8*, 152. [CrossRef]
22. Zhang, H.; Wu, W.; Chen, Z.; Jing, J. Well Logs Reconstruction of Petroleum Energy Exploration Based on Bidirectional Long Short-Term Memory Networks with a PSO Optimization Algorithm. *Geoenergy Sci. Eng.* **2024**, *239*, 212975. [CrossRef]
23. He, Z.; Shao, H.; Zhong, X.; Zhao, X. Ensemble Transfer CNNs Driven by Multi-Channel Signals for Fault Diagnosis of Rotating Machinery Cross Working Conditions. *Knowl.-Based Syst.* **2020**, *207*, 106396. [CrossRef]
24. Wang, K.; Ma, C.; Qiao, Y.; Lu, X.; Hao, W.; Dong, S. A Hybrid Deep Learning Model with 1DCNN-LSTM-Attention Networks for Short-Term Traffic Flow Prediction. *Phys. A Stat. Mech. Its Appl.* **2021**, *583*, 126293. [CrossRef]
25. Niu, Z.; Zhong, G.; Yu, H. A Review on the Attention Mechanism of Deep Learning. *Neurocomputing* **2021**, *452*, 48–62. [CrossRef]
26. Guo, J.; Lv, H.; Zhao, Q.; Yang, Y.; Zhu, Z.; Zhang, Z. CNN-GRU-ATT Method for Resistivity Logging Curve Reconstruction and Fluid Property Identification in Marine Carbonate Reservoirs. *J. Mar. Sci. Eng.* **2025**, *13*, 331. [CrossRef]
27. Lin, L.; Wei, H.; Wu, T.; Zhang, P.; Zhong, Z.; Li, C. Missing Well-Log Reconstruction Using a Sequence Self-Attention Deep-Learning Framework. *Geophysics* **2023**, *88*, D391–D410. [CrossRef]
28. Liao, W.; Gao, C.; Fang, J.; Zhao, B.; Zhang, Z. A TCN-BiGRU Density Logging Curve Reconstruction Method Based on Multi-Head Self-Attention Mechanism. *Processes* **2024**, *12*, 1589. [CrossRef]
29. Chen, Y.; Zhang, D. Theory-Guided Deep-Learning for Electrical Load Forecasting (TgDLF) via Ensemble Long Short-Term Memory. *Adv. Appl. Energy* **2021**, *1*, 100004. [CrossRef]

30. Jia, J. Identification of Water-Flooded Layers and Evaluation of Flooded Levels in Fractured Tight Sand Oil Reservoir. *Processes* **2024**, *12*, 2467. [CrossRef]
31. Wang, F.; Zhao, L.; Bian, H.; Tan, C.; Li, J. Identification of Watered-out Zones in Carbonate Reservoirs Using Resistivity Curve Reconstruction Based on Reservoir Classification. *Energy Geosci*. **2023**, *4*, 100092. [CrossRef]
32. Xu, W.; Zhang, Z.; Lv, H.; Zeng, W.; Meng, S. Lithology-Constrained Adaptive Inversion of Original Formation Resistivity for Water-Flooded Reservoir Evaluation. *J. Appl. Geophys*. **2026**, *253*, 106418. [CrossRef]
33. Zhang, H.; Zhang, Z.; Nie, X.; Zhang, C.; Lv, H.; Yan, W. A New Method of Identification of Water-Flooded Layers Based on HistGBDT Algorithm—A Case of the Penglai 19-3 Oilfield. *Processes* **2025**, *13*, 3219. [CrossRef]

Disclaimer/Publisher's Note: The statements, opinions and data contained in all publications are solely those of the individual author(s) and contributor(s) and not of MDPI and/or the editor(s). MDPI and/or the editor(s) disclaim responsibility for any injury to people or property resulting from any ideas, methods, instructions or products referred to in the content.